Classification: BIOLOGICAL SCIENCES: Neuroscience

Title: Endothelial CXCL5 negatively regulates myelination and repair after white matter stroke

Authors: Guanxi Xiao[1], Rosie Kumar[1], Jasmine Burguet[2], Yutaro Komuro[1], Visesha Kakarla[1], Christopher K. Williams[3], Xinhai R. Zhang[3], Michal Macknicki[1], Andrew Brumm[1], Riki Kawaguchi[1,4], Harry V. Vinters[3], S. Thomas Carmichael[1], Leif A. Havton[1,5], Charles DeCarli[6], Jason D. Hinman[1,*]

Affiliations:

[1] Department of Neurology, David Geffen School of Medicine, University of California Los Angeles

[2] Institut Jean-Pierre Bourgin, INRA, AgroParisTech, CNRS, Université Paris-Saclay, 78000 Versailles, France

[3] Department of Neuropathology, David Geffen School of Medicine, University of California Los Angeles

[4] Department of Psychiatry, Semel Institute for Neuroscience and Human Behavior, University of California Los Angeles

[5] Department of Neurobiology, David Geffen School of Medicine, University of California Los Angeles

[6] Department of Neurology, University of California Davis

*To whom correspondence should be addressed:

Jason D. Hinman, M.D., Ph.D.

Department of Neurology

David Geffen School of Medicine

University of California Los Angeles

635 Charles E. Young Dr. South, Room 415

Los Angeles, CA 90095

Ph: 310-825-6761

Email: jhinman@mednet.ucla.edu

Keywords: CXCL5, cerebral small vessel disease, obesity, white matter, stroke

Abstract:

Cerebral small vessel disease and resulting white matter pathologies are worsened by cardiovascular risk factors including obesity. The molecular changes in cerebral endothelial cells caused by chronic cerebrovascular risk factors remain unknown. We developed a novel approach for molecular profiling of chronically injured cerebral endothelial cells using cell-specific translating ribosome affinity purification (RiboTag) with RNA-seq in Tie2-Cre:RiboTag mice. We used this approach to identify the transcriptome of white matter endothelial cells after the onset of diet-induced obesity (DIO). DIO induces an IL-17B signaling pathway that acts on the cerebral endothelia through IL-17Rb leading to increased endothelial expression of CXCL5 in both the DIO mouse model and in aged humans where cerebral small vessel disease is common. In the white matter, endothelial CXCL5 acts as a chemoattractant and promotes the association of oligodendrocyte progenitor cells (OPCs) with cerebral endothelia increasing vessel-associated OPC cell number and surface area. Targeted blockade of IL-17B with peripheral antibody administration reduced the population of vessel-associated OPCs by reducing endothelial CXCL5 expression. CXCL5-mediated sequestration of OPCs to white matter vasculature impairs OPC differentiation after a focal white matter ischemic lesion. DIO promotes a unique white matter endothelial-to-oligodendrocyte progenitor cell signaling pathway that compromises brain repair after stroke.

Significance Statement: Chronic cardiovascular risk factors damage cerebral small vessels yet the molecular pathways induced in injured cerebral endothelial cells that lead to tissue injury are unknown. Obesity-induced endothelial expression of CXCL5 in brain white matter disrupts normal myelination by forcing oligodendrocyte progenitor cells to associate with the cerebral vasculature and impedes brain repair after stroke.

Text:

Introduction

Cerebral small vessel disease is an age-related entity affecting brain white matter. The resulting white matter lesions accumulate over time (1) and contribute to disability (2), dementia (3-5), and death (6). Cerebral small vessel injury is significantly worsened by chronic cardiovascular risk factors such as hypertension, diabetes, and obesity (7-10). In particular, abdominal obesity and its associated metabolic disturbances in blood pressure, lipids, and blood sugar control increase the risk of developing white matter lesions on MRI (11-14) and increase the likelihood of lacunar brain infarction or stroke (15). While the pathologic changes associated with cerebral small vessel disease are well known (16, 17), the molecular pathways that drive small vessel injury in the brain are largely unknown.

Emerging data suggests that an interaction between cerebral vessels and cells of the oligodendrocyte lineage play a key role in maintaining white matter homeostasis (18-20). A subset of platelet-derived growth factor receptor alpha-positive (PDGFRα+) oligodendrocyte progenitor cells (OPCs) closely associate with the vasculature (21) and use it to migrate in the brain during development (22). Proteins secreted by endothelial cells promote OPC migration and proliferation *in vitro* (23, 24). In the spontaneously hypertensive rat model of cerebral small vessel disease, the OPC population is increased in association with vascular changes and delays in OPC maturation may be mediated by endothelial secretion of *HSP90α* (25). Both the diagnosis and treatment of cerebral small vessel disease would be advanced by identifying additional molecular pathways active in cerebral endothelia and driven by chronic cardiovascular risk factors (26).

To identify the molecular changes in white matter endothelia in the setting of chronic cardiovascular risk factors, we used a mouse model of diet-induced obesity (DIO) (27) that recapitulates a number of features of human cardiovascular risk (28). We demonstrate that DIO is associated with a loss of white matter vasculature, increases in the number of OPCs in brain white matter, thinner myelin, and disrupted axons. We used cell-specific translating ribosome affinity purification and RNA-sequencing in Tie2-Cre:RiboTag mice to isolate the endothelial-specific transcriptome after the onset of DIO. Pathway analysis of the top up-regulated genes indicates that DIO induces an IL-17B signaling pathway that acts on the cerebral endothelia through the up-regulation of IL-17Rb leading to increased endothelial expression of CXCL5. Endothelial expression of CXCL5 is increased in cerebral white matter vessels of aged humans. In the mouse model, endothelial over-expression of CXCL5 directly signals to OPCs acting as a chemoattractant *in vivo*. DIO-induced endothelial expression of this immune signaling pathway exacerbates the white matter injury response to a focal white matter ischemic lesion and restricts the maturation of OPCs during the repair phase after stroke. These findings indicate that DIO promotes cerebral endothelial inflammation and through the expression of CXCL5 exerts vascular regulation of myelination by sequestering the main progenitor cell of the adult brain, the OPC, to blood vessels. This pathway has direct implications for the understanding of human cerebral small vessel disease and repair of cerebral white matter.

Results

Diet-induced obesity as a model of white matter and vascular injury

Obesity is a significant risk factor for the development of small vessel disease and white matter injury (10, 11, 13, 14). We used a well-established model of diet-induced obesity (DIO) (27) to model the effects of chronic cardiovascular risk on brain white matter and the vasculature. Beginning at 8 weeks of age, mice were fed a control fat diet (CFD) or a high fat diet (HFD) for 12 weeks. After 12 weeks on the dietary intervention, mice exhibit 84% weight gain and metabolic disturbances in cholesterol and blood sugar (Fig. S1) broadly consistent with the diagnostic criteria for metabolic syndrome (29). After the development of obesity, we examined the vasculature and cellular makeup of the white matter.

Using a Tie2-Cre;tdTomato (Ai14) strain that robustly labels the vasculature throughout the brain, we characterized the effects of DIO on the white matter vasculature throughout the corpus callosum (Fig. 1A). DIO reduces the volume of tdT+ vessels by 26.0% and the branch complexity of the vasculature (Fig. 1B). DIO also resulted in an increase in the PDGFRα+ oligodendrocyte progenitor cells (OPCs) within the corpus callosum and a concordant increase in OPCs associated with vessels, measured as OPCs per unit vessel length (Fig. 1C-D). Consistent with a DIO-induced increase in OPCs, we observed fewer and shorter axonal paranodal segments (Fig. S2A) as well as thinner myelin with an increased g-ratio as measured by electron microscopy (Fig. S2B), indicating compromise of white matter integrity in DIO mice. We developed a direct RNA hybridization assay for oligodendrocyte staging based on overall marker gene expression patterns in white matter, clustered by the three main stages of oligodendrocyte development. The top 40 genes marking OPCs, pre-myelinating oligodendrocytes (PMO), and

myelinating oligodendrocytes (MO) (30) were used to indicate oligodendrocyte stages in mice on Using this 120 gene expression platform (Supplemental Data File 1; Fig. 1E, Fig. S2C), we found an increase in OPC gene expression in DIO white matter, with animals on HFD clustering more closely with genetically defined OPCs, consistent with light microscopy findings. Together, these findings suggested that DIO increases OPC proliferation, increases the number of OPCs associated with vessels, and biases the oligodendrocyte lineage towards immaturity.

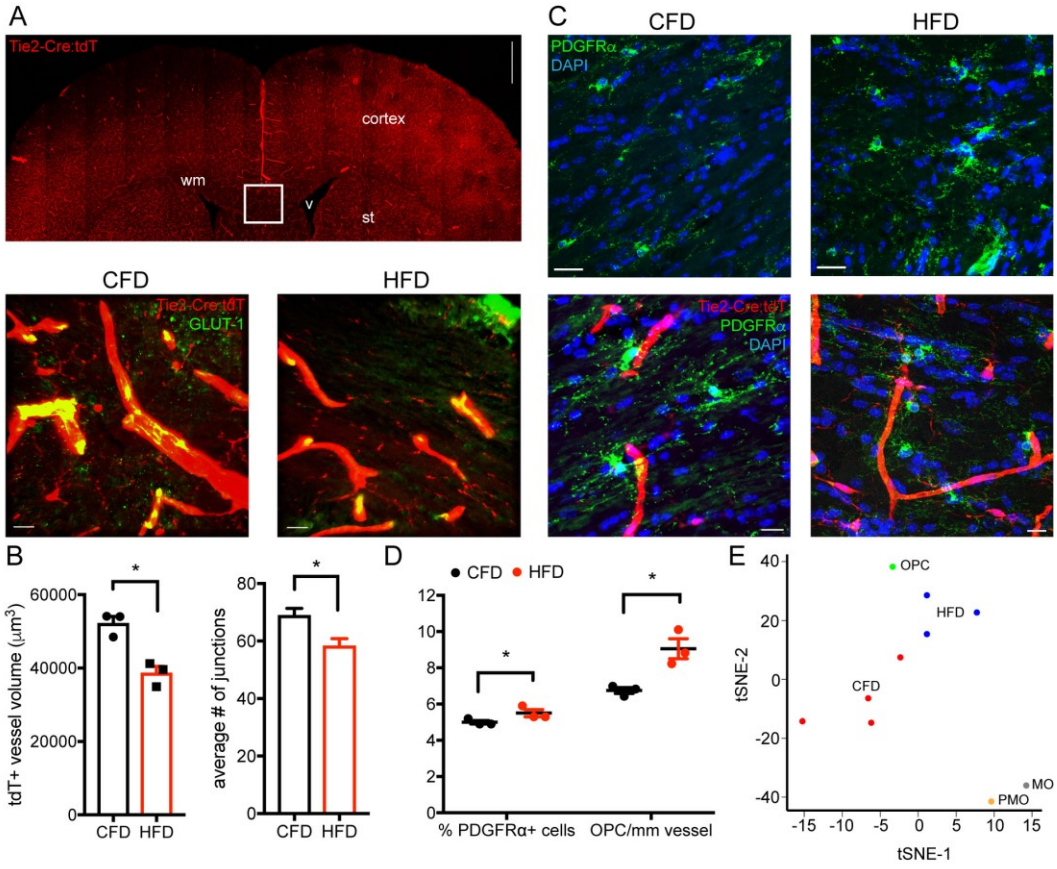

Figure 1. Diet-induced obesity as a model of white matter and vascular injury.

Tie2-Cre;tdTomato transgenic mice (*n*=3/grp; 15 confocal z-stacks per animal; inset box) were used to measure vascular changes after DIO (A). Images of white matter from CFD (left lower panel) and HFD (right lower panel) animals labeled for Tie2-Cre;tdTomato (red) and GLUT-1 (green). Average white matter tdT+ vessel volume in CFD (black) and HFD (red) animals (p=0.0069; left) and average vascular junctions (p=0.0032; right) (B). PDGFRα+ OPCs (green) in CFD (left upper panel) and HFD (right upper panel) white matter. Vessel-associated PDGFRα+ OPCs in CFD (left lower panel) and HFD (right lower panel) (C). Percentage of PDGFRα+ OPCs is increased in HFD (5.01±0.13% vs. 5.66±0.22%; *p=0.014) and the number

of PDGFRα+ OPCs per mm vessel length in increased (6.46±0.23 vs. 8.94±0.31 cells/mm; *p<0.0001) (D). tSNE of Nanostring gene expression for CFD (red, n=4) and HFD (blue, n=3) animals using reference profiles of OPCs, pre-myelinating oligodendrocytes (PMO), and myelinating oligodendrocytes (MO). Scale bars = 10 μm.

Molecular profiling of white matter endothelia

Systemic cardiovascular risk factors such as DIO exert their effect on white matter by primarily damaging the cerebrovasculature. To identify the molecular pathways induced in white matter endothelia, we developed an approach using Tie2-Cre:RiboTag mice together with translating ribosome affinity purification using the RiboTag method (31) (Fig. 2A). This transgenic approach leads to robust HA labeling in the cerebrovasculature (Fig. 2B). HA-immunoprecipitated RNA using this approach shows endothelial specificity, with a specific enrichment of endothelial transcripts (Fig. 2C) compared to established marker genes for pericytes and OPCs (30). DIO results in a specific gene expression profile compared to endothelial cells from normal weight mice (Fig. S3A; SI Data File 2) within white matter endothelia: 112 genes are up-regulated and 60 genes are down-regulated (FDR<0.1, Fig. 2D). Gene ontology of the up-regulated genes suggests enrichment of immune signaling pathways including C-X-C chemokine signaling and interleukin receptor activation (Fig. S3B). Among the top differentially regulated genes, *interleukin-17 receptor b* (*IL17Rb*) (8.83-fold increased, FDR=0.090) and its effector chemokine *Cxcl5* (11.35-fold increased, FDR=0.064) were two of the most strongly up-regulated genes when comparing DIO vs. control animals (Fig. 2E).

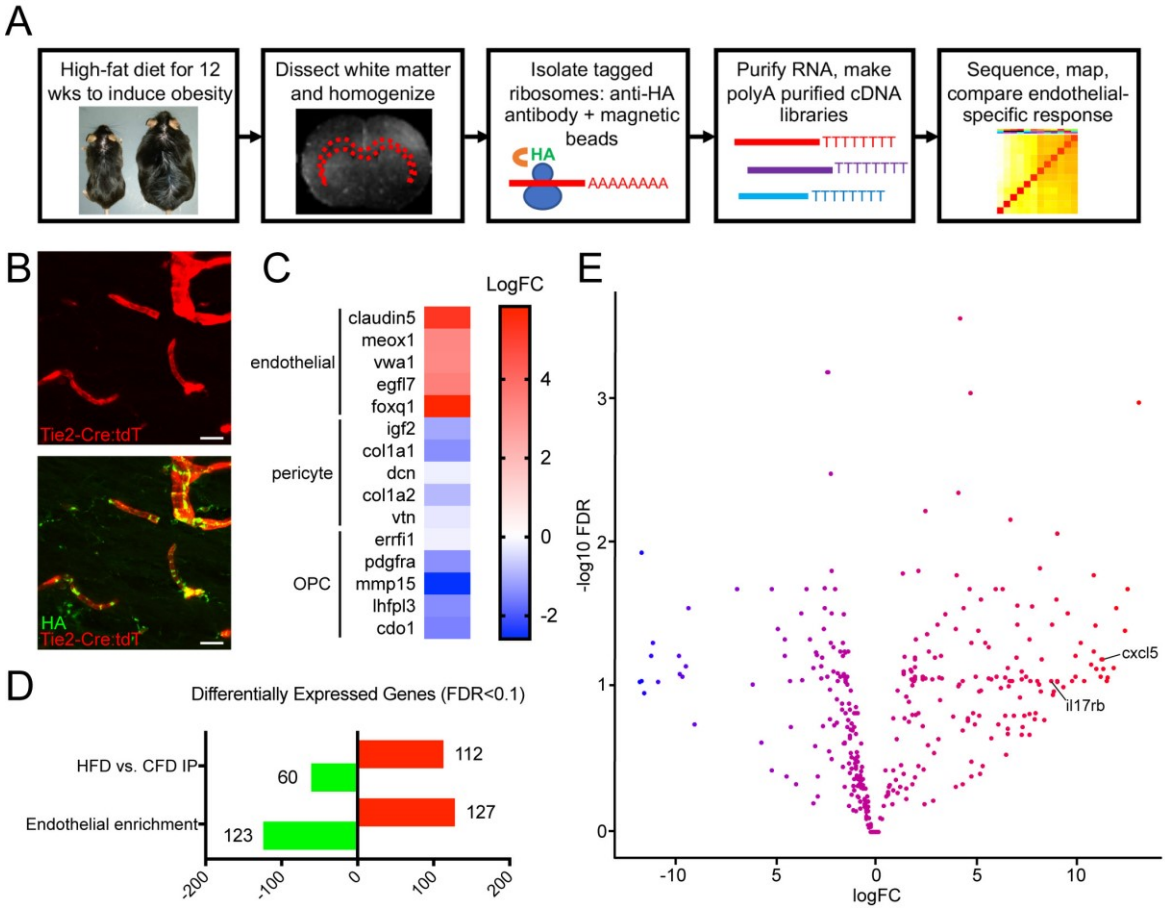

Figure 2. Molecular profiling of white matter endothelia.

Schematic representation of workflow for identifying the molecular profile of chronically injured white matter endothelia using translating ribosome affinity purification after DIO (A). Tie2-Cre;tdTomato;RiboTag transgenic mice labeled for HA (B). Anti-HA pulldowns from control white matter show enrichment for endothelial marker genes and de-enrichment of pericyte and OPC markers (C). Differentially expressed genes (FDR<0.1) between anti-HA pulldowns in CFD and HFD animals (n=3/grp) and IP vs. input in CFD animals showing the number of genes up- and down-regulated in endothelial in normal weight mice (D). Volcano plot of the top differentially expressed genes between anti-HA pulldowns in CFD and HFD with *Il17rb* and *Cxcl5* labeled. Scale bars = 10 μm. Complete gene list available in SI Data File 2.

IL-17Rb and CXCL5 up-regulation in human and murine white matter vasculature

IL-17 signaling involves five interleukin ligands (A-E) and five cognate receptor isoforms that hetero and/or homo-dimerize to effect downstream signaling (32). Within our transcriptional dataset, the only IL-17 receptor isoform that was significantly differentially regulated in DIO-

affected cerebral endothelial cells was IL-17Rb (Table S1). Among a number of diverse functions, IL-17 receptor signaling activates effector chemokine signaling, including CXCL5 (33) as a mechanism of identifying tissue injury. CXCL5 is a member of the C-X-C chemokine family (34) acts a chemoattractant in other tissues and has been reportedly up-regulated in white matter after peri-natal hypoxia (35). Guided by our RNA-seq data, we hypothesized that DIO may induce IL-17B signaling acting through IL-17Rb resulting in increased endothelial expression of CXCL5 (Fig. 3A). To confirm RNA-seq results, we performed TRAP-qPCR using independent Tie2-Cre:RiboTag biologic replicates for a subset of differentially regulated genes (*Glut-1, Itgb3*, *Cd180, Hsd3b3, Tnfrsf10b, Il17rb, Cxcl5, and Ttc21a* **)** (Fig. 3B). Similar degrees of up-regulation for *Il17rb* and *Cxcl5* using qPCR were seen. Retro-orbital venous blood sampling confirmed increased serum detection of CXCL5 in DIO mice (Fig. 3C). Immunofluorescent labeling for IL-17Rb (Fig. 3D) and CXCL5 (Fig. 3E) in Tie2-Cre;tdTomato (Ai14) mice demonstrated a marked increase in detection of both molecules within white matter cerebral vessels in DIO mice.

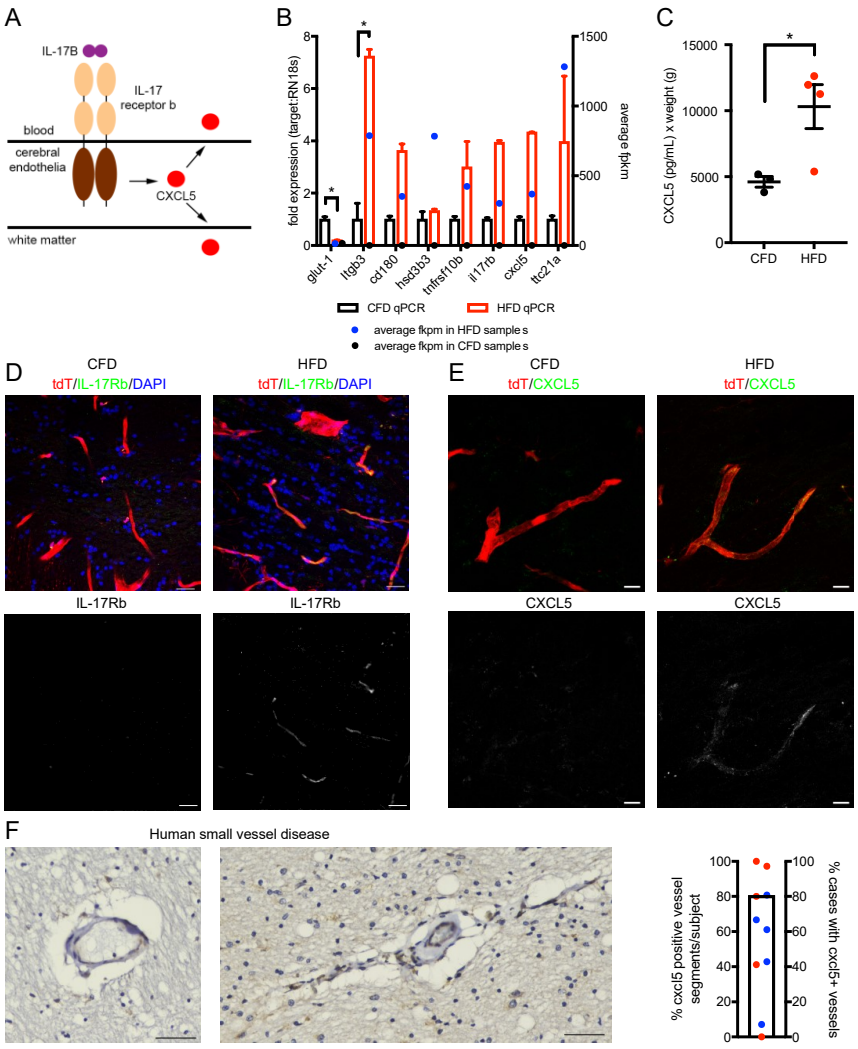

Figure 3. IL-17Rb and CXCL5 up-regulation in injured white matter vasculature. Schematic representation of IL-17/CXCL5 signaling in chronically injured cerebral endothelia (A). TRAP-qPCR confirmation of RNA-sequencing results for selected genes in independent Tie2-Cre:RiboTag mice (n=2/grp) (*p<0.05) (B). Weight adjusted-ELISA values (pg/mL) for murine CXCL5 in retro-orbital blood samples from CFD (black) and HFD (red) animals (n=4/grp, p=0.0355) (C). Immunofluorescence labeling for IL-17Rb (green, D) and CXCL5 (green, E) is absent in white matter vasculature of Tie2-Cre;tdTomato mice on CFD (left panels) and abundant in white matter vasculature of Tie2-Cre;tdTomato mice on HFD (right panels). Single channel labeling for IL17Rb (lower panels, D) and CXCL5 (lower panels, E) show heterogenous endothelial expression. CXCL5 is detected in human frontal white matter endothelia from aged subjects. Bar represents percentage of cases (8/10) with any CXCL5 staining with points indicating the individual percentage of CXCL5-positive vessel segments in individuals with (blue) and without (red) vascular dementia (F). Scale bars = 50 μm in F, 20 μm in D, 10 μm in E.

To verify the relevance of this DIO-induced cerebrovascular molecular pathway to human cerebral small vessel disease, we examined endothelial CXCL5 expression in a series of older (86±8 years of age) human post-mortem specimens with (n =5) and without (n =5) a pathologic diagnosis of cerebral vascular disease sufficient to influence cognition in the setting of low levels of Alzheimer's disease pathology. All subjects with vascular disease had combined evidence of macro- and microscopic cerebral vascular disease (Table S2). Sections containing frontal peri-ventricular white matter were immunolabeled for CXCL5 (Fig. S4). In this older cohort, CXCL5 is robustly detected in cerebral vessel segments within white matter, with 80% demonstrating at least some CXCL5 staining within white matter vasculature, while the mean percentage of vessel segments showing CXCL5 staining was 71.2±0.08% (17.2±3.4 vessel segments/subject) (Fig. 3F). In this small aged cohort, white matter vessel CXCL5-positivity did not associate with a clinical diagnosis of vascular dementia. However, most, if not all individuals living to his age have some degree of frontal white matter injury indicating that small vessel disease is nearly ubiquitous at advanced age. In fact, 70% of these cases had pathologic evidence of cerebral vascular injury (Table S2).

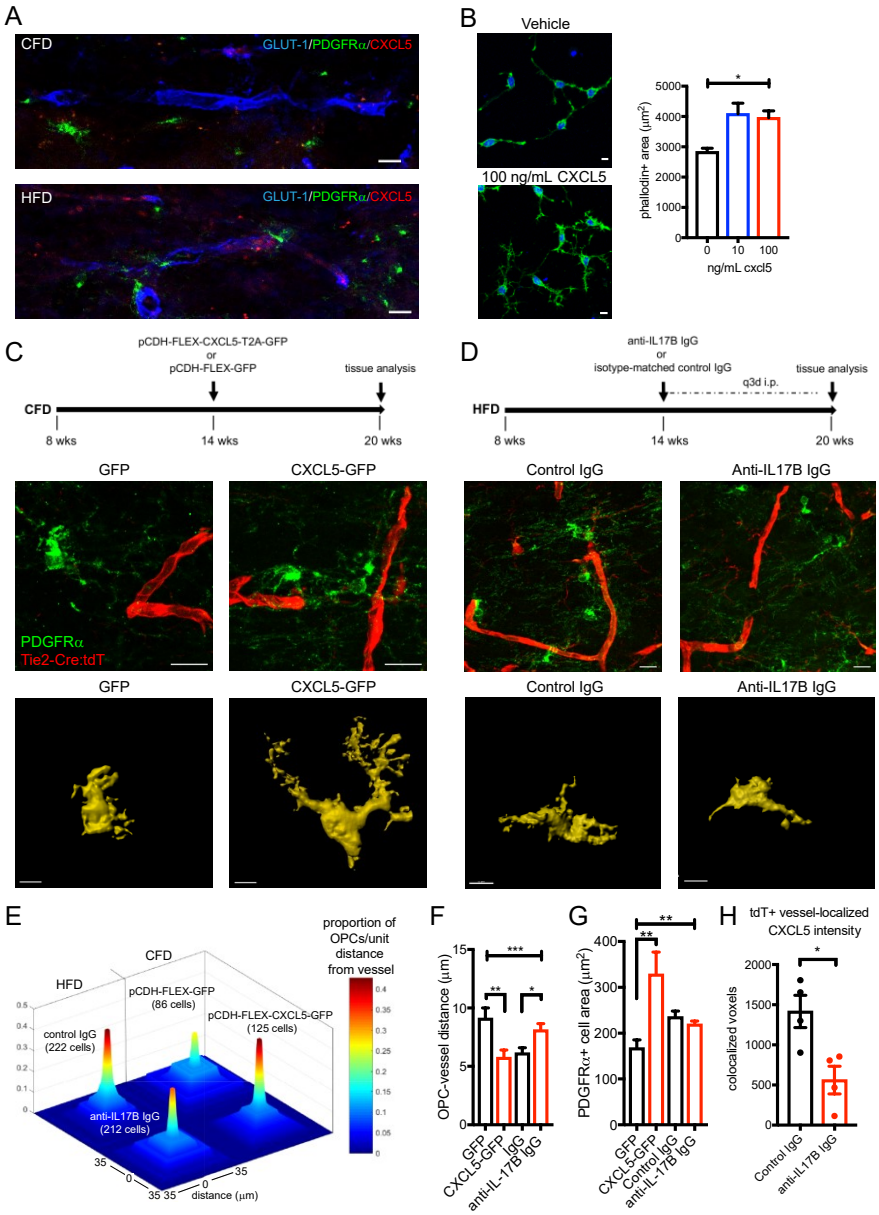

Figure 4. CXCL5 is a novel vessel-to-OPC signal in white matter vasculature. Association of PDGFRα+ OPCs (green) with the vasculature (blue) in CFD (upper panel) and CXCL5-positive (red) HFD animals (lower panel) (A). Phalloidin-positive cellular area in O4+ OPCs grown in vitro exposed to vehicle (upper panel) or recombinant CXCL5 (lower panel) for 48 h (p<0.0001, F=9.82 by one-way ANOVA). Experimental approach for CXCL5 transgenic-viral gain of function (upper panel, C). PDGFRα+ OPC (green) labeling in GFP-transduced Tie2-Cre;tdTomato mice (red, left panel) and CXCL5-GFP-transduced Tie2-Cre;tdTomato mice (right panel). Representative masked cellular profiles of PDGFRα+ cell area (lower panels). Schematic of anti-IL-17B antibody treatment (upper panel, D). PDGFRα+ OPC (green) labeling in control IgG-treated Tie2-Cre:tdT mice (left panel) and anti-IL-17B IgG-treated Tie2-Cre:tdT mice (right panel). Representative masked cellular profiles of PDGFRα+ cell area (lower panels). Proportion of OPCs per unit distance from vessel (0-35 μm) in each condition (total measured cell number per condition in parentheses) (E). Average distance of OPCs to vessel (***p=0.0005, F=6.06 by one-way ANOVA; **adjusted p=0.0039; *adjusted p=0.0168) (F).

Average *in vivo* PDGFRα+ OPC cell area (***p*=0.0068, F=7.38 by one-way ANOVA; **adjusted *p*=0.002) (G). Graph of co-localized CXCL5+/GLUT-1+ voxels in anti-IL-17B IgG-treated animals (*n*=4/grp; **p*=0.018). (H). Scale bars = 10 μm.

The IL-17/CXCL5 pathway as a novel vessel-to-OPC signaling paradigm

With the known role of chemokine receptor (CXCR) signaling on OPC migration (22), we reasoned that endothelial up-regulation of CXCL5 in DIO mice may function to promote OPC migration to the vasculature. To this end, we observed a notable increase in OPCs that were in close apposition to CXCL5+ vessel segments (Fig. 4A) in DIO mice. *In vitro* exposure of O4+ OPCs to increasing doses of recombinant murine CXCL5 resulted in a dose-dependent increase in OPC cell area with cytoskeletal changes suggesting motility (Fig. 4B). To determine the ability of endothelial CXCL5 to signal to OPCs *in vivo*, we used a combined transgenic and targeted viral gene expression approach (Fig. 4C). We designed a pCDH-FLEX-CXCL5-T2A-GFP lentiviral construct and injected this virus into the subcortical white matter of Tie2-Cre;tdTomato mice resulting in targeted gene expression specifically in white matter vasculature (Fig. S5). After 6 weeks of endothelial up-regulation of CXCL5-GFP or GFP in normal weight mice, we measured the distance of individual OPCs from vessels and the cell area of vessel-associated OPCs (Fig. S6), as well as the number of OPCs per unit vessel length (Fig. S7). The average distance of OPCs from tdT+ vessels was reduced in CXCL5-GFP injected animals compared to GFP injected animals while the number of PDGFRα+ OPCs in apposition to tdT+ vessels were increased (upper panels Fig. 4C, 4E, 4F) supporting a chemoattractant role for CXCL5 on OPCs. Similar to the effects of recombinant CXCL5 on OPCs *in vitro*, endothelial over-expression of CXCL5 *in vivo* resulted in increased OPC cell area (lower panels Fig. 4C, 4G).

To block DIO-induced endothelial CXCL5 expression resulting from IL-17Rb activation, we employed repetitive peripheral injections of a function-blocking anti-IL-17B antibody or isotype control IgG for 6 weeks in Tie2-Cre;tdTomato mice on HFD (Fig. 4D, S1D). Endothelial CXCL5 expression within the tdT+ vasculature was reduced by 60.4% using this approach (Fig. 4H) while IL-17Rb levels were not changed (Fig. S8) indicating that DIO-induced increases in endothelial CXCL5 can be at least partially regulated through IL-17B signaling at the endothelial cell surface. Peripheral blocking of IL-17B signaling significantly reduced the association of OPCs with the cerebral vasculature in DIO mice (upper panels Fig. 4D, 4E, 4F). Vessel-associated OPC cell area was not significantly different in HFD mice administered anti-IL-17B antibody (lower panels Fig. 4D, Fig. 4G), suggesting additional HFD-associated pathways drive the regulation of OPC cell area.

Endothelial CXCL5 exaggerates the OPC response to focal white matter ischemia and impedes remyelination after stroke

To determine the consequence of endothelial CXCL5 on injury response after focal white matter ischemia, we used an established model of white matter stroke (36, 37) (Fig. 5A) that produces a distinct population of stroke-responsive PDGFRα+ OPCs (38). At 7d after white matter stroke, there was no significant difference in the stroke lesion volume comparing animals on CFD vs. HFD (Fig. S9). To determine the role that DIO-induced endothelial CXCL5 expression influences injury response after focal white matter ischemia, we labeled for GLUT-1 and CXCL5 at 7d post-stroke. We measured the percentage of CXCL5+ voxels that co-localized with GLUT-1 within the peri-infarct tissue surrounding the stroke (Fig. S10). As in uninjured white matter, the percentage of CXCL5+/GLUT-1+ voxels were significantly increased within the peri-infarct

tissue in animals on HFD (Fig. 5B). Immunofluorescent labeling for PDGFRα+ OPCs identified an increase in stroke-responsive OPCs per lesion in DIO mice compared to control (Fig. 5C) at 7d post-stroke. Spatial mapping of stroke-responsive OPCs coupled with nearest neighbor comparative analysis (Fig. S11) indicates a greater distribution of stroke-responsive OPCs that specifically occurs at the lesion margins in DIO mice compared to control (Fig. 5D) where endothelial CXCL5 levels were increased. This increase is at least partially accounted for by an increased association of OPCs with CXCL5+ vessel segments within the peri-lesional tissue. This DIO-induced OPC-vessel interaction in the early phase impacts repair after stroke. At 28d after stroke, we compared PDGFRα+ OPC and GST-π+ mature oligodendrocyte cell counts in three regions of interest spanning the ischemic white matter lesion. This analysis revealed a significant change in oligodendrocyte cell populations 28d after stroke (p=0.0011, two-way ANOVA, F=14.47) (Fig. 5E). An increased number of residual stroke-responsive PDGFRα+ OPCs were present at 28d post-stroke in animals on HFD compared to CFD (adjusted p=0.0114). The number of GST-π+ mature oligodendrocytes within the lesion at 28d post-stroke was variable and generally reduced in animals on HFD compared to CFD (adjusted p=0.0654).

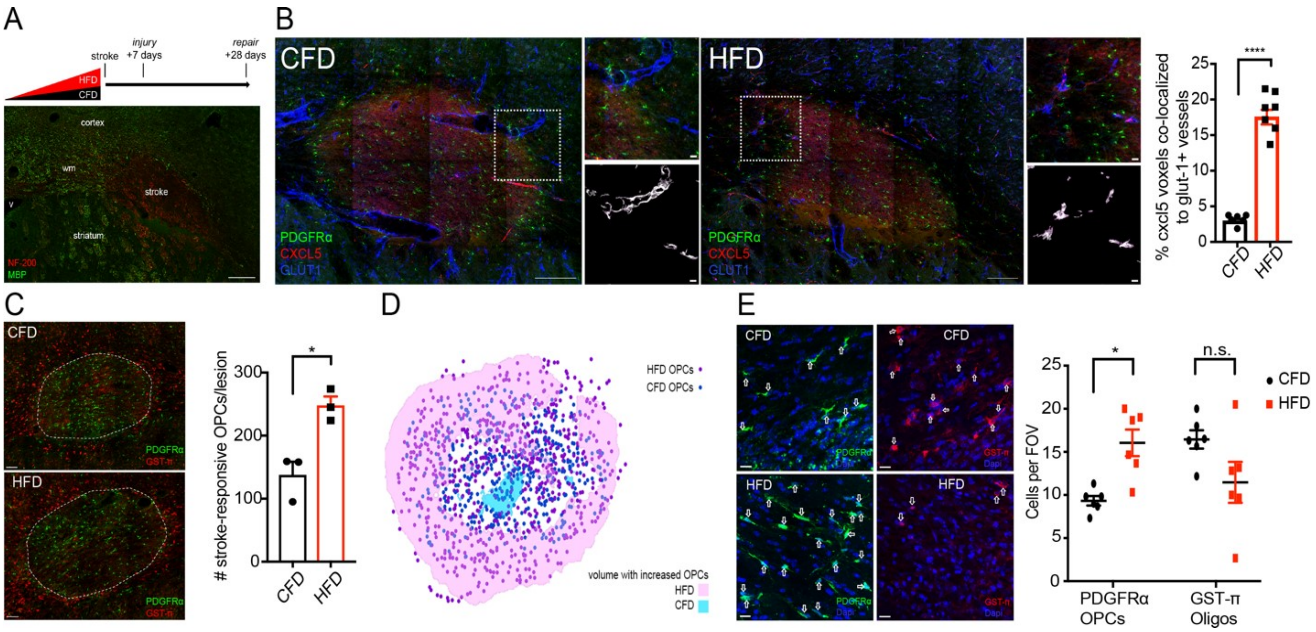

Figure 5. DIO-induced changes in stroke-responsive OPCs and repair after focal white matter stroke.

Schematic of stroke modeling in animals on CFD and HFD (upper panel) with a representative white matter ischemic lesion shown with labeling for myelin basic protein (MBP, green) and neurofilament-200 (NF-200, red) (A). Labeling for GLUT-1 (blue), CXCL5 (red), and PDGFRα (green) at 7d post-stroke in animals on CFD (left) and HFD (right). Insets boxes from the peri-infarct tissue (upper) masked for GLUT-1 (white) with only co-localized CXCL5 (purple) (lower). Graph of percentage of co-localized CXCL5+/GLUT-1+ voxels (****p<0.0001) (B). Labeling of stroke-responsive PDGFRα+ OPCs (green) and GST-π (red) mature oligodendrocytes at 7d post-stroke and graph of #OPCs/lesion (C). Spatial mapping of stroke-responsive OPCs in CFD (dark blue) and HFD (purple) with shaded areas indicated regions of stroke lesion with statistically increased stroke-responsive OPCs between CFD (light blue) and HFD (pink) (D). Representative images from stroke-lesions at 28d post-stroke labeled for PDGFRα+ OPCs (green, left) and GST-π mature oligodendrocytes (red, right) between CFD (upper) and HFD (lower) animals with DAPI labeling of cell nuclei (blue). Graph of oligodendrocyte cell numbers at 28d post-stroke (*p=0.0114) (E). Scale bars = 10 μm.
CFD and HFD.

Discussion

Cerebral small vessel disease is increasingly recognized as a substantial contributor to stroke risk and dementia (39). Microvascular injury in the brain is driven by cardiovascular risk factors yet molecular factors that link systemic vascular risk factors with molecular pathways in the brain are lacking. Obesity is a major cardiovascular and cerebral vascular risk factor, is growing prevalence (40), is associated with white matter changes in humans (11, 13-15), and has a reliable animal model (27). Using a diet-induced obesity model, we show that obesity reduces white matter vasculature and increases OPCs in chronically injured white matter, as reported in other models (25). Our results showing ultrastructural changes in myelin in adult onset diet-induced obesity are similar to those seen in genetically obese (ob/ob) mice with reductions in myelin (41) and increases in OPCs in leptin-deficient ob/ob mice (42) validating this model for the study of chronic white matter injury. The present findings are the first to identify the transcriptome of chronically injured cerebral endothelia. We used that dataset to identify disordered vascular signaling that acts to regulate OPCs and impairs remyelination after stroke.

Cell-specific transcriptional profiling using ribosomal tagging is a valuable tool in parsing out molecular signals from a complex tissue such as the brain (31, 43). Here, we developed a methodology to profile cerebral endothelial cells *in vivo*. By combining this vascular Ribotag mouse with a chronic vascular risk factor model, we identified novel endothelial pathways that appear relevant to human cerebral small vessel disease. A similar vascular profiling approach could be easily applied to identify microvascular injury signals in other organs such as the kidney or retina. It could also be applied to other chronic or acute neurologic conditions that feature microvascular injury including aging, diabetes, or isolated hypertension. Such efforts to better characterize the molecular pathways relevant to human cerebral small

vessel disease is crucial for the development of diagnostic and therapeutic interventions (26). While we focused on the paracrine effects of chronically injured endothelial cells and signaling into the white matter, the identification of the endothelial response to chronic cerebrovascular risk factors may also facilitate the development of novel fluid-based biomarkers to track the response of the cerebral endothelium to chronic risk factors.

Vessels and OPCs are known to interact both during development and to maintain white matter homeostasis (44). During CNS development, OPCs migrate extensively to distribute throughout the entire CNS and this migration requires the physical vascular scaffold (22). Cerebral endothelial cells secrete trophic factors that activate Src and Akt signaling pathways to support the survival and proliferation of OPCs (18). However, the full spectrum of molecular pathways that drive the vessel-OPC interaction remain largely unknown. The present data in disease and studies in the developing brain indicate that chemokines are critical. In-vivo time lapse imaging reveals that in the developing mouse brain, OPCs interact with vasculature and migrate along the vessels to the destined cerebral regions dependent on CXCR4 activation in OPCs, which binds to endothelial secreted ligand CXCL12, and promotes their attraction to cerebral vasculature (45). Our study illustrates a similar phenomenon, with DIO-induced endothelial expression of CXCL5 promoting the association of OPCs to the vasculature within adult white matter *in vivo*. These results further imply that chemokine signaling pathways play a significant role in regulating the interaction between endothelial cells (ECs) and OPCs that is critical to white matter maintenance and the response to injury.

What is the consequence of sequestering OPCs to the vascular bed? In the spontaneously hypertensive rat model of cerebral small vessel disease in which endothelial cells are progressively injured, OPCs are increased and fail to mature properly. In this model,

dysfunctional endothelial cells impair the maturation of OPCs *in vitro* and promote their proliferation through the production of HSP90α (25). In the DIO mouse model, we observed a reduction in white matter microvascular complexity with the surviving endothelial cells responding with a specific transcriptional response implicating growth factor and immune signaling. In part, this response appears to cause OPCs to respond to vascular injury through CXCL5 signaling to OPCs. These OPCs are elongated along vessels with a long leading edge or display hypertrophied cell bodies and processes compared to those OPCs that are not associated with blood vessels, similar to those previously reported for migratory or reactive OPCs (22, 23, 46). These migratory or reactive OPCs are likely responding to disrupted vascular integrity but as a result of their new restriction to the vascular bed, fail to properly differentiate, ultimately compromising remyelination after stroke. This disordered vascular regulation of myelination provides a new concept in understanding cellular signaling in cerebral small vessel disease. Though we clearly demonstrate that CXCL5 can serve as this vascular injury regulatory signal in rodents and humans, further studies are needed to definitively prove whether this response serves some partially protective role on the blood-brain barrier through reciprocal OPC to endothelial signaling (47).

White matter ischemic lesions are characterized by a robust early loss of axons, myelin and oligodendrocytes (48-50). Similar to inflammatory white matter lesions (51), OPCs respond early and robustly to white matter ischemic lesions common to the aging human brain (38, 49, 52). The peri-infarct white matter at the margin of the ischemic lesion, often referred to as the white matter penumbral region (53), is where cross-talk between axons and oligodendrocytes is compromised (55, 56). Here, we used a novel approach to identify the spatial relationship of stroke-responsive OPCs to a focal white matter stroke lesion. This approach directly informs our

data by showing that the increase in stroke-responsive OPCs produced by obesity occurs precisely in the peripheral margins of the white matter stroke lesion where tissue repair and the stimuli for remyelination would be maximal. In DIO mice, the stroke-responsive OPC lesion area is 30% larger and this expanded penumbral region is marked by increased endothelial CXCL5 expression explaining why more stroke-responsive OPCs are seen at the lesion periphery. The consequence of this is apparent at 28 days after stroke; DIO-induced endothelial expression of CXCL5 leaves behind a population of activated, injury-responsive OPCs whose maturation is inhibited. This progenitor restricted state could indicate that remyelination is simply delayed after stroke or it could lead to a progressive dysfunctional OPC response as the ability of NG2+ OPCs to differentiate into oligodendrocytes declines with chronic insults (57).

From our data, an emerging concept places the cerebral endothelial cell at the center of the pathophysiology relevant to cerebral small vessel disease. As the conduit between the brain and systemic insults such as hypertension, diabetes, and the metabolic disturbances of obesity, identifying molecular pathways in the cerebral endothelia represent a yet incompletely-realized target for understanding disease pathogenesis. With the tools described here, the molecular pathways activated in cerebral endothelia can now be deeply characterized. Changes in normal white matter homeostasis that result from chronic cerebrovascular risk factors can directly alter injury response and repair after stroke by acting through vascular regulation of myelination. That the pathway we characterized is functionally absent from normal young adult mice yet ubiquitous in aged human samples suggests greater efforts to appropriately model co-morbid conditions in animal models of stroke and cerebrovascular injury may pave a smoother path to translation into human trials.

Material and Methods

Animals

Mice were housed under UCLA regulation with a 12-hour dark-light cycle. All animal studies presented here were approved by the UCLA Animal Research Committee ARC#2014-067-01B, accredited by the AAALAC. Diet-induced obesity was induced in mice by ad lib feeding with 60%kCal from fat chow (HFD) or 10%kCal from fat chow (CFD) (Research Diets, Inc.). Weights (g) were measured weekly. Mice strains used in this study are described in *SI Materials and Methods.*

Translating ribosome affinity purification and RNA-sequencing

HA-tagged ribosomal associated RNAs from cerebral white matter endothelia were isolated and purified by Nucleospin miRNA kit (Machary-Nagel). RNA-sequencing was run using 69 bp paired end reads. Reads were aligned to the mouse genome using STAR (v.mm10). Differential gene expression analysis was performed using EdgeR assuming an FDR <0.1 as significant. Gene ontology analysis was performed using Enrichr (58). Additional information of RNA isolation, RNA sequencing and analysis are described in *SI Materials and Methods*.

Immunofluorescence and Confocal Imaging

Animals were euthanized with a lethal dose of isoflurane, transcardially perfused with PBS followed by 4% paraformaldehyde in 0.1 M sodium phosphate buffer, brains removed, post-fixed for 24 hrs and cryoprotected for 48 hrs in 30% sucrose in PBS. Forty microns coronal cryosections and immunostaining was performed essentially as described (36). Details regarding antibodies and microscopic imaging are available in *SI Materials and Methods*. Human post-

mortem brain sections were selected from the UC Davis ADC Neuropathology Core samples based on *a priori* selection criteria and stained for CXCL5/6 using standard immunohistochemistry.

White matter stroke

Subcortical white matter ischemic injury was induced as previously described (37) using three stereotactic injections of L-Nio (L-N^5-(1-Iminoethyl) ornithine, dihydrochloride; Calbiochem) into the subcortical white matter under sensorimotor cortex. Animals (n = 4/grp) were sacrificed at 7- or 28-days post-stroke and analyzed for tissue outcomes.

Lentiviral Injection

A dual promoter lentiviral backbone was created through sequential subcloning to place either GFP or murine CXCL5 between loxP sites. Control GFP and CXCL5-GFP lentivirus were packaged in human 293 cells (ATCC cat. no. CRL-11268) and concentrated by ultracentrifugation on a sucrose column. 200 nL of concentrated virus was injected into the subcortical white matter and allowed to express for 6 weeks.

Anti-IL-17B Antibody Administration

Anti-mIL-17B function blocking antibody (R&D, AF1709) was diluted with 0.9% saline to a concentration of 1mg/ml. Normal Goat isotype-matched IgG (R&D, AB-108-C) was used as control. Tie2-Cre;tdTomato mice were fed with high fat diet starting at 8 weeks old and weighed weekly. Aliquots of 50µg of anti-mIL-17B IgG or control IgG were prepared and administered in a blinded fashion every 72 hours by intraperitoneal injection from 14 weeks old and analyzed 48 hours after the last injection at 20 weeks old.

Statistical Analysis

The number of animals used in each experiment is listed in the Results section or Figure Legend. Statistical analysis was performed using GraphPad Prism 7 software. Unless otherwise stated, statistical significance was determined using α=0.05, corrected for multiple comparisons. Data are shown as mean ± SEM.

Other Methods

Further details regarding procedures related to gene expression and analysis, immunohistochemistry, electronic microscopy, spatial analysis, and statistical analysis are explained in detail in *SI Materials and Methods*. All DNA sequences, primers, plasmids and packaged viruses are available upon request. Gene expression data is available in the *SI Data Files*.

Author contributions:

G.X., Ro.K., and J.D.H. designed research and collected data; G.X., Ri.K., Y.K., and J.D.H. performed gene expression analysis; G.X. and J.B. performed spatial analysis; G.X., L.A.H., and J.D.H. performed electron microscopy and analysis; A.B., M.M, S.T.C., and J.D.H performed lentiviral cloning and packaging; C.K.W, X.R.Z, H.V.V., V.K, G.X, and C.D. performed human brain tissue selection, staining, and analysis; G.X. and J.D.H. wrote the paper.

Acknowledgments:

The authors are grateful to Kelsey Ericson for preparation of human brain tissue specimens.

This work was graciously supported by grants from the Larry L. Hillblom Foundation (TLLHF 2014-A-014), the American Heart Association Grant-in-Aid (16GRNT31080021). LAH and STC receive support from the Dr. Miriam and Sheldon G. Adelson Medical Research Foundation. CD receives support from UC Davis Alzheimer's Disease Center grant P30 AG 010129. JDH receives support from the National Institute for Neurological Disorders and Stroke (K08 NS083740) and the United States Department of Veterans Affairs Greater Los Angeles Healthcare System.

References

1. Gouw AA, *et al.* (2008) Progression of white matter hyperintensities and incidence of new lacunes over a 3-year period: the Leukoaraiosis and Disability study. *Stroke* 39(5):1414-1420.
2. Inzitari D, *et al.* (2009) Changes in white matter as determinant of global functional decline in older independent outpatients: three year follow-up of LADIS (leukoaraiosis and disability) study cohort. *BMJ* 339:b2477.
3. Jokinen H, *et al.* (2011) Incident lacunes influence cognitive decline: the LADIS study. *Neurology* 76(22):1872-1878.
4. Koga H, *et al.* (2009) Cognitive consequences of multiple lacunes and leukoaraiosis as vascular cognitive impairment in community-dwelling elderly individuals. *J Stroke Cerebrovasc Dis* 18(1):32-37.
5. Reed BR, *et al.* (2004) Effects of white matter lesions and lacunes on cortical function. *Arch Neurol* 61(10):1545-1550.
6. Debette S & Markus HS (2010) The clinical importance of white matter hyperintensities on brain magnetic resonance imaging: systematic review and meta-analysis. *BMJ* 341:c3666.
7. van Dijk EJ, *et al.* (2004) The association between blood pressure, hypertension, and cerebral white matter lesions: cardiovascular determinants of dementia study. *Hypertension* 44(5):625-630.
8. de Leeuw FE, *et al.* (2002) Hypertension and cerebral white matter lesions in a prospective cohort study. *Brain* 125(Pt 4):765-772.
9. Jongen C, *et al.* (2007) Automated measurement of brain and white matter lesion volume in type 2 diabetes mellitus. *Diabetologia* 50(7):1509-1516.
10. Manschot SM, *et al.* (2006) Brain magnetic resonance imaging correlates of impaired cognition in patients with type 2 diabetes. *Diabetes* 55(4):1106-1113.
11. Bokura H, Yamaguchi S, Iijima K, Nagai A, & Oguro H (2008) Metabolic syndrome is associated with silent ischemic brain lesions. *Stroke* 39(5):1607-1609.
12. Park K & Yasuda N (2009) Association between metabolic syndrome and minimal leukoaraiosis. *Stroke* 40(1):e5; author reply e6.
13. Park K, *et al.* (2008) Significant associations of metabolic syndrome and its components with silent lacunar infarction in middle aged subjects. *J Neurol Neurosurg Psychiatry* 79(6):719-721.
14. Yin ZG, *et al.* (2014) Association between metabolic syndrome and white matter lesions in middle-aged and elderly patients. *Eur J Neurol* 21(7):1032-1039.
15. Kwon HM, *et al.* (2009) Significant association of metabolic syndrome with silent brain infarction in elderly people. *J Neurol* 256(11):1825-1831.
16. Fisher CM (1979) Capsular infarcts: the underlying vascular lesions. *Arch Neurol* 36(2):65-73.
17. Esiri MM, Wilcock GK, & Morris JH (1997) Neuropathological assessment of the lesions of significance in vascular dementia. *J Neurol Neurosurg Psychiatry* 63(6):749-753.
18. Arai K & Lo EH (2009) An oligovascular niche: cerebral endothelial cells promote the survival and proliferation of oligodendrocyte precursor cells. *J Neurosci* 29(14):4351-4355.
19. Pham LD, *et al.* (2012) Crosstalk between oligodendrocytes and cerebral endothelium contributes to vascular remodeling after white matter injury. *Glia* 60(6):875-881.
20. Maki T, *et al.* (2015) Potential interactions between pericytes and oligodendrocyte precursor cells in perivascular regions of cerebral white matter. *Neurosci Lett* 597:164-169.
21. Marques S, *et al.* (2016) Oligodendrocyte heterogeneity in the mouse juvenile and adult central nervous system. *Science* 352(6291):1326-1329.
22. Tsai HH, *et al.* (2016) Oligodendrocyte precursors migrate along vasculature in the developing nervous system. *Science* 351(6271):379-384.
23. Hayakawa K, *et al.* (2011) Vascular endothelial growth factor regulates the migration of oligodendrocyte precursor cells. *J Neurosci* 31(29):10666-10670.

24. Hayakawa K, *et al.* (2012) Cerebral endothelial derived vascular endothelial growth factor promotes the migration but not the proliferation of oligodendrocyte precursor cells in vitro. *Neurosci Lett* 513(1):42-46.
25. Rajani RM, *et al.* (2018) Reversal of endothelial dysfunction reduces white matter vulnerability in cerebral small vessel disease in rats. *Sci Transl Med* 10(448).
26. Corriveau RA, *et al.* (2017) Alzheimer's Disease-Related Dementias Summit 2016: National research priorities. *Neurology* 89(23):2381-2391.
27. Surwit RS, Kuhn CM, Cochrane C, McCubbin JA, & Feinglos MN (1988) Diet-induced type II diabetes in C57BL/6J mice. *Diabetes* 37(9):1163-1167.
28. Kennedy AJ, Ellacott KL, King VL, & Hasty AH (2010) Mouse models of the metabolic syndrome. *Dis Model Mech* 3(3-4):156-166.
29. Huang PL (2009) A comprehensive definition for metabolic syndrome. *Dis Model Mech* 2(5-6):231-237.
30. Zhang Y, *et al.* (2014) An RNA-sequencing transcriptome and splicing database of glia, neurons, and vascular cells of the cerebral cortex. *J Neurosci* 34(36):11929-11947.
31. Sanz E, *et al.* (2009) Cell-type-specific isolation of ribosome-associated mRNA from complex tissues. *Proc Natl Acad Sci U S A* 106(33):13939-13944.
32. Gaffen SL (2009) Structure and signalling in the IL-17 receptor family. *Nat Rev Immunol* 9(8):556-567.
33. Chen K, *et al.* (2016) IL-17 Receptor Signaling in the Lung Epithelium Is Required for Mucosal Chemokine Gradients and Pulmonary Host Defense against K. pneumoniae. *Cell Host Microbe* 20(5):596-605.
34. Strieter RM, *et al.* (1995) The functional role of the ELR motif in CXC chemokine-mediated angiogenesis. *J Biol Chem* 270(45):27348-27357.
35. Wang LY, Tu YF, Lin YC, & Huang CC (2016) CXCL5 signaling is a shared pathway of neuroinflammation and blood-brain barrier injury contributing to white matter injury in the immature brain. *J Neuroinflammation* 13:6.
36. Hinman JD, Rasband MN, & Carmichael ST (2013) Remodeling of the axon initial segment after focal cortical and white matter stroke. *Stroke* 44(1):182-189.
37. Nunez S, *et al.* (2016) A Versatile Murine Model of Subcortical White Matter Stroke for the Study of Axonal Degeneration and White Matter Neurobiology. *J Vis Exp* (109).
38. Sozmen EG, *et al.* (2016) Nogo receptor blockade overcomes remyelination failure after white matter stroke and stimulates functional recovery in aged mice. *Proc Natl Acad Sci U S A* 113(52):E8453-E8462.
39. Debette S, Schilling S, Duperron MG, Larsson SC, & Markus HS (2018) Clinical Significance of Magnetic Resonance Imaging Markers of Vascular Brain Injury: A Systematic Review and Meta-analysis. *JAMA Neurol*.
40. Services USDoHH (2018) Nutrition, Physical Activity, and Obesity: Data, Trends and Maps.
41. Sena A, Sarlieve LL, & Rebel G (1985) Brain myelin of genetically obese mice. *J Neurol Sci* 68(2-3):233-243.
42. Udagawa J, Nimura M, & Otani H (2006) Leptin affects oligodendroglial development in the mouse embryonic cerebral cortex. *Neuro Endocrinol Lett* 27(1-2):177-182.
43. Heiman M, Kulicke R, Fenster RJ, Greengard P, & Heintz N (2014) Cell type-specific mRNA purification by translating ribosome affinity purification (TRAP). *Nat Protoc* 9(6):1282-1291.
44. Arai K & Lo EH (2009) Oligovascular signaling in white matter stroke. *Biol Pharm Bull* 32(10):1639-1644.
45. Banisadr G, *et al.* (2011) The role of CXCR4 signaling in the migration of transplanted oligodendrocyte progenitors into the cerebral white matter. *Neurobiol Dis* 44(1):19-27.
46. Hampton DW, Rhodes KE, Zhao C, Franklin RJ, & Fawcett JW (2004) The responses of oligodendrocyte precursor cells, astrocytes and microglia to a cortical stab injury, in the brain. *Neuroscience* 127(4):813-820.

47. Seo JH, *et al.* (2014) Oligodendrocyte precursor cells support blood-brain barrier integrity via TGF-beta signaling. *PLoS One* 9(7):e103174.
48. Back SA, *et al.* (2007) Hypoxia-ischemia preferentially triggers glutamate depletion from oligodendroglia and axons in perinatal cerebral white matter. *J Cereb Blood Flow Metab* 27(2):334-347.
49. Sozmen EG, Kolekar A, Havton LA, & Carmichael ST (2009) A white matter stroke model in the mouse: axonal damage, progenitor responses and MRI correlates. *J Neurosci Methods* 180(2):261-272.
50. Valeriani V, Dewar D, & McCulloch J (2000) Quantitative assessment of ischemic pathology in axons, oligodendrocytes, and neurons: attenuation of damage after transient ischemia. *J Cereb Blood Flow Metab* 20(5):765-771.
51. Tripathi RB, Rivers LE, Young KM, Jamen F, & Richardson WD (2010) NG2 glia generate new oligodendrocytes but few astrocytes in a murine experimental autoimmune encephalomyelitis model of demyelinating disease. *J Neurosci* 30(48):16383-16390.
52. Miyamoto N, *et al.* (2015) Astrocytes Promote Oligodendrogenesis after White Matter Damage via Brain-Derived Neurotrophic Factor. *J Neurosci* 35(41):14002-14008.
53. Maillard P, *et al.* (2011) White matter hyperintensity penumbra. *Stroke* 42(7):1917-1922.
54. Reimer MM, *et al.* (2011) Rapid disruption of axon-glial integrity in response to mild cerebral hypoperfusion. *J Neurosci* 31(49):18185-18194.
55. Hinman JD, Lee MD, Tung S, Vinters HV, & Carmichael ST (2015) Molecular disorganization of axons adjacent to human lacunar infarcts. *Brain* 138(Pt 3):736-745.
56. Rosenzweig S & Carmichael ST (2015) The axon-glia unit in white matter stroke: mechanisms of damage and recovery. *Brain Res* 1623:123-134.
57. Mason JL, *et al.* (2004) Oligodendrocytes and progenitors become progressively depleted within chronically demyelinated lesions. *Am J Pathol* 164(5):1673-1682.
58. Gundersen GW, *et al.* (2015) GEO2Enrichr: browser extension and server app to extract gene sets from GEO and analyze them for biological functions. *Bioinformatics* 31(18):3060-3062.

Supporting information

Title: Endothelial CXCL5 negatively regulates myelination and repair after white matter stroke

Authors: Guanxi Xiao[1], Rosie Kumar[1], Jasmine Burguet[2], Yutaro Komuro[1], Visesha Kakarla[1], Christopher K. Williams[3], Xinhai R. Zhang[3], Michal Macknicki[1], Andrew Brumm[1], Riki Kawaguchi[1,4], Harry V. Vinters[3], S. Thomas Carmichael[1], Leif A. Havton[1,5], Charlie DeCarli[6], Jason D. Hinman[1,*]

[*] *To whom correspondence should be addressed:

Jason D. Hinman, M.D., Ph.D.

David Geffen School of Medicine

University of California Los Angeles

Department of Neurology

635 Charles E. Young Dr. South, Room 415

Los Angeles, CA 90095

Ph: 310-825-6761

Email: jhinman@mednet.ucla.edu

Materials and methods

Animals

Wild-type C57Bl/6 mice fed ad lib on 60%kCal from fat chow (HFD) (Strain #380050) or 10%kCal from fat chow (CFD) (Strain #380056) were purchased directly from Jackson Labs at 17 weeks of age and allowed to acclimate for 2 weeks prior to experimental use. The Tie2-Cre;tdTomato mice were generated by crossing Tie2-Cre mice with flox-stop tdTomato mice (Jackson Labs Strain #007908 – B6;129S6-Gt(ROSA)26Sor$^{tm14(CAG-tdTomato)Hze}$/J).

Immunofluorescence

Animals were euthanized with a lethal dose of isoflurane, transcardially perfused with PBS followed by 4% paraformaldehyde in 0.1 M sodium phosphate buffer, brains removed, post-fixed for 24 hrs and cryoprotected for 48 hrs in 30% sucrose in PBS. Forty microns coronal cryosections and immunostaining was performed essentially as described [1]. The following primary antibodies were used: mouse anti-NF200 (1:200, Sigma), rabbit anti-MBP (1:500, Calbiochem), goat anti-PDGFRα (1:500; Neuromics), mouse anti-HA (1:1000, Biolegend), rabbit anti-AnkG (1:1000, Dako), rabbit anti-$Na_V1.6$ (1:250), rabbit-Gst-π (1:1000, Millipore), rat anti-IL-17Rb (1:500, Santa Cruz Biotech), rat anti-CXCL5 (1:250, R&D) in PBS containing 5% goat or donkey serum and 0.3% Triton-X 100 (Sigma) overnight at 4°C. Secondary antibody labeling was performed using donkey anti-mouse, donkey anti-rabbit, or donkey anti-goat Fab_2-Alexa conjugated antibodies (Jackson Immunoresearch, Inc.).

Immunohistochemistry for human brain samples

Case selection was made from a subset of 950 UC Davis ADC Neuropathology Core samples based on *a priori* selection criteria. In this case, we selected 5 cognitively normal individuals with low Braak and Braak scores and 5 demented subjects with low Braak and Braak scores that also had evidence of cerebrovascular disease sufficient to cause dementia. To be most consistent with current diagnostic criteria, we selected the most recent cases available based on the selection criteria. Immunohistochemistry was performed using formalin (Medical Chemical Corporation, 575A) fixed paraffin embedded tissue sections cut at 6µm. Sections where placed on positive charged slides (Fisherbrand, 12-550-15) then incubated overnight at 60 °C. De-paraffinization was accomplished with three 5min xylene (Fisher Scientific, X3P) washes. The samples were rehydrated with graded concentrations of alcohol (American MasterTech, ALREACS) diluted with deionized water. Endogenous peroxidase was blocked with a 3% solution of hydrogen peroxide (Fisher Scientific, H325-500) 20min incubation. Heat-induced epitope retrieval used a citrate buffer (BioCare Medical, CB910M). The slides incubated in the buffer at 90°C for 45min. Blocking used 2.5% normal horse serum (Vector, S2012) for 60min. Antigen specificity was elucidated by incubating the slides for 90min in CXCL5/6 (1:100, Abcam, ab198505). Primary antibody detection was amplified with a 45min incubation using a secondary antibody (Vector, MP-7401). A 5 seconds counterstain used hematoxylin (Richard Allan Scientific, 7221). The samples were dehydrated with graded alcohols and three xylene washes before being coverslipped.

Microscopy and microscopic analysis

All microscopic images were obtained using a Nikon C2 confocal microscope. Tie2-Cre;tdTomato expressing vessels were used for the analyses of vessel volume, vessel length and

junction point. Vessel volume was measured by Imaris software with automated "Add surface" function. Volume of small particle less than 30μm^3 was subtracted to eliminate the background interference. Vessel length and junction point were analyzed by AngioTool [2]. The parameters for AngioTool measurement were set as "Diameter 5-40", "Intensity 40-255" and "Particles less than 10000".

The size of PDGFRα+ OPC was measured individually by Imaris automated "Add surface" function. Voxel of small particle less than 800 was subtracted to eliminate the background interference. OPC-vessel distance was measured by Imaris with "Add spot" function. For PDGFRα+ OPC location, nucleus with Dapi staining was used as a reference. The distance of Tie2-Cre;tdTomato vessel to PDGFRα+ OPC was measured with the function of "Spot to Spot closest distance".

OPC number and x,y,z positional coordinates were analyzed by Imaris "Add spot" function. OPCs stroke responsive areas were generated by Imaris "Add Surface" function. Measurements of stroke areas were generated using Fiji [3]. Representative images were selected for presentation.

The levels of CXCL5/IL-17Rb in anti-IL-17B/IgG treated mice white matter were measured by Imaris "Coloc" function. The percentages of CXCL5/IL-17Rb that colocalized with Tie2cre;tdTomato positive vessels were measured as voxel areas. For GLUT-1/CXCL5 colocalization measurement, GLUT-1 positive vessels were masked by Imaris with "Add surface" to create new GLUT-1 and CXCL5 channels. The percentages of GLUT-1/CXCL5 colocalization in new channels were measured as voxel areas by Imaris "Coloc" function.

Electron microscopy

Wild-type C57Bl/6 mice (*n* =6/grp) on CFD or HFD were transcardially perfused with a 2% glutaraldehyde solution, post-fixed for 24 hrs, hemisected in the sagittal plane and 2 mm cubes including the corpus callosum were dissected and embedded in plastic resin for ultrastructural analysis as previously described [4]. One micron, plastic embedded toluidine blue stained sections were used to select transcallosal fibers underneath sensorimotor cortex by light microscopy. Three electron micrographs were obtained at a primary magnification of 7200X using a JEOL 100 CX transmission electron microscope and a representative electron micrograph of high technical quality from each animal was used for quantitation of fiber diameter, axon diameter, myelin thickness, and g-ratio.

Translating ribosome affinity purification and RNA-sequencing

After 12 weeks on CFD or HFD, Tie2-Cre:RiboTag mice (*n* = 3 per group) were sacrificed and the subcortical white matter was freshly dissected and immediately placed into buffer with RNase inhibitors. A tissue homogenate was generated using a 1mL sequential glass homogenizer. HA-tagged ribosomes from cerebral white matter endothelia were isolated following the established RiboTag protocol [5] using equal volumes of tissue homogenate. Total RNA was isolated from both input and IP samples using the Nucleospin miRNA kit (Machary-Nagel). Normalized RNA amounts (ng) underwent cDNA library generation using the TrueSeq with Ribozero kit preparation (Illumina), pooled and sequenced using 69 bp paired end reads. Samples were sequenced over 4 lanes for an average of read count of 62.1 ± 10.7 million per sample. Reads were aligned to the mouse genome using STAR (v.mm10). Differential gene expression analysis was performed using EdgeR assuming an FDR <0.1 as significant. Gene ontology analysis was performed using Enrichr [6].

Nanostring gene expression

Using established oligodendrocyte stage marker genes [7], we designed a custom Nanostring gene expression array (XT_GX CodeSet Oligostg #116000651) using gene-specific probes for each the 40 genes marking each oligodendrocyte stage (OPC, pre-myelinating oligodendrocyte (PMO), and myelinating oligodendrocyte (MO)). C57Bl/6 mice (n=4/group) were maintained on 12 weeks of CFD or HFD. At 20 weeks of age, the corpus callosum was isolated, homogenized, and RNA using the Nucleospin miRNA kit (Clontech) to collect both large and small RNA species. RNA was quantitated and 100 ng of RNA from each animal was provided as input for the direct RNA detection assay. Manufacturer protocol was followed and the results were analyzed using nCounter software. Results were normalized and differentially expressed genes were compared individually between groups using a Student's t-test ($p<0.05$). The number of DEGs ($p<0.05$) per stage was determined. log2FC values were calculated as a function of averaged housekeeping gene expression levels (*actb, b2m, gapdh, pgk1, rpl19*). To generate an oligodendrocyte stage cell type index, raw gene expression values were combined with FPKM values from Zhang et al. (2014) and normalized by rank. Hierarchal clustering analysis was performed using hclust and tSNE plots (perplexity=3, max iteration = 5000) generated using standard algorithms. The resulting classification and 2-dimensional representation were highly reproducible.

Lentiviral preparation, packaging, and injection

A plasmid containing the open reading frame of the murine CXCL5 sequence with a 3' stop codon was purchased from Origene (#MR200761). The pCDH-EF1-FLEX-EGFP-CMV-2A-TagBFP2-SC dual promoter lentiviral backbone was created by subcloning the FLEX-GFP sequence between the loxP sites from the pAAV-FLEX-GFP vector (Addgene #28304) into the

pCDH-EF1-MCS-CMV-2A-pTagBFP2-SC dual promoter lentiviral construct using restriction digestion. The pCDH-EF1-FLEX-EGFP-CMV-2A-TagBFP2-SC backbone was linearized by removing the GFP sequence between the loxP sites using restriction digestion with XhoI and EcoRI (New England Biolabs). The murine CXCL5 sequence was PCR amplified in a HiFi DNA Assembly reaction (New England Biolabs) such that it was subcloned in the 3'>5' position in between the loxP sites. The resulting reaction was transformed into Stbl3 E.coli cells and positive clones were identified by restriction digestion and verified by DNA sequencing. Subsequently, a 3'>5' T2A-copGFP sequence was added 5' to the murine CXCL5 sequence. The donor T2A-copGFP vector (pCDH-EF1-MCS-copGFP; System Biosciences) was PCR amplified and subcloned into pCR-Blunt II TOPO (ThermoFisher Scientific) for amplification and utilized in a HiFi DNA Assembly reaction. The resulting reaction was transformed as above and positive clones were identified by restriction digestion and DNA sequencing. DNA amplification was performed using an Endotoxin-Free PureLink Plasmid Midiprep Kit (ThermoFisher Scientific). Resulting DNA was quantified and used in lentiviral packaging. All DNA sequences, primers, plasmids and packaged viruses are available upon request.

T175 flasks were coated with Poly-L-Lysine for about 20min and allowed to air dry completely. $2.3x10^7$ 293T/17cells (ATCC cat. no. CRL-11268) were seeded into each T175 flask and cultured with 30 ml DMEM (Gibco cat.no. 11960-044)/10% FBS (Thermo Fisher HyClone SH30071.03) overnight with 3% CO_2 at 37°C. Fresh DMEM/10% FBS was exchanged 4 hours before transfection. Four plasmids (60 µg pCDH-FLEX-CXCL5-GFP or pCDH-FLEX-GFP expression vector, 39 µg pMDLg/pRRE packing, 15 µg pRSV-REV plasmid and 21 µg pMD2.G envelope) were mixed with 0.750 ml of 1M $CaCl_2$ and water to a total volume of 3 ml/tube. After filtering through a 0.2µm syringe filter, 2.8 ml of 2xBES (50 mM N,N-bis[2-hydroxyethyl]-2-

aminoethanesulfonic acid, 280 mM NaCl, 1.5 mM Na_2HPO_4; pH 6.96) was added to a 2.7 ml of DNA/plasmids mixture in 14ml polystyrene tube and incubated on a vortex mixer for 15 minutes at room temperature. After incubation, DNA/plasmids mixture were transferred to a T175 flask, swirled gently and incubate at 37°C for 16 hours with 3% CO_2. After overnight incubation, cells were washed with 1XPBS and incubated with fresh 28 ml DMEM/10%FBS and 10 mM sodium butyrate for 24 hours with 3% CO_2. Supernatant was collected, centrifuged at 1500 RPM for 10 min and filtered through 0.45 μm filter. Virus supernatant was centrifuged at 20000 RPM for 2 hours 25 min and resuspended in 2 ml DPBS (Fisher cat.no. MT-21-031-CM). The resuspended supernatant was then loaded on 20% sucrose column and centrifuged at 32000 RPM for 2 hours 25 min. After centrifugation, the supernatant was discarded and the viral pellet was gently resuspended in 40 – 100 μl of DPBS. The virus suspension was transferred to a sterile Eppendorf tube and centrifuged at 7000 RPM for 5 min. Virus was aliquoted without disturbing the pellet and stored at -80°C.

Two stereotactic injections (A/P:0.55, M/L1.95, D/V:-1.30; A/P1.10, M/L:1.75, D/V: -1.35) of 200 nL pCDH-FLEX-CXCL5-GFP or pCDH-FLEX-GFP were injected into subcortical white matter at 14 weeks old Tie2-Cre;tdTomato mice and allowed to express for 6 weeks. Animals were maintained with control fat diet and analyzed at 20 weeks old.

Spatial analysis

Analysis of the spatial distribution of stroke-responsive OPCs was performed as follows. The boundary of increased PDGFR-α-+ cells and the loss of GST-π-+ cells was identified in each of three sections per animal (n=3 animals/group). Using Imaris software, the x,y,z position of each PDGFR-α-+ cell relative to the user defined center point (x=0, y=0, z=0) of the elliptical

stroke region was determined. Because the z-axis was limited (10 μm), a two-dimensional grid analysis was performed using a 2D modification of the previously reported 3D spatial density estimator [8] using a smoothing parameter of k=8. The local cell density in each position within the overlaid grid is compared statistically as previously described [9]. Therefore, a p-value map is generated for each position in the grid and thresholded (p<0.05) to reveal regions with significant density differences.

Statistics

The number of animals used in each experiment is listed in the Results section. Oligodendrocyte population cell counts as a fraction of total cells were determined by averaging counts from 5 fields of view throughout the corpus callosum across a minimum of three sections 240 μm apart. Per animal averages were generated and significance between groups determined using an unpaired Welch's t-test (α=0.05). Analysis of nodal/paranodal complexes was performed using an unpaired Welch's t-test (α=0.05), while paranodal length varies based on axonal diameter and was therefore analyzed using a distribution analysis and Chi-square statistic (df=12). Measurements of white matter ultrastructural features were averaged across animals and each feature was compared separately using Mann-Whitney U test between groups (α=0.05). Gene expression differences generated by Nanostring were determined at the individual gene level using unpaired Welch's t-test (α=0.05). Determination of stroke lesion area was performed by sampling lesion area (n=3-5 40 μm sections) across groups (n=4/grp) and using the sampled distribution to create bootstrapped area distribution (n=25) representing a full area sampling of the approximate 1 mm lesion created by the stroke model. This area distribution was averaged across animals in each group and compared using a Mann-Whitney U test between groups

(α=0.05). Spatial analysis of stroke-responsive OPCs were determined as detailed above. Cell counts at 28d post-stroke were determined across three sections 240 μm apart with lesion core and edge analyses determined using a two-way ANOVA (α=0.05) with post-hoc Holm-Sidak test to adjust *p*-values for multiple t-tests. Statistical analysis was performed using GraphPad Prism 7 software. Data are shown as mean ± SEM.

Study approval

All animal studies presented here were approved by the UCLA Animal Research Committee ARC#2014-067-01B, accredited by the AAALAC. All human subjects were involved in the UCD ADC longitudinal study IRB # 215830-46. Written informed consent for autopsy was obtained from the subject or next of kin prior to examination.

Data and materials availability: All DNA sequences, primers, plasmids and packaged viruses are available upon request. Gene expression data is available in the Supplemental Data Files.

Supplemental figures

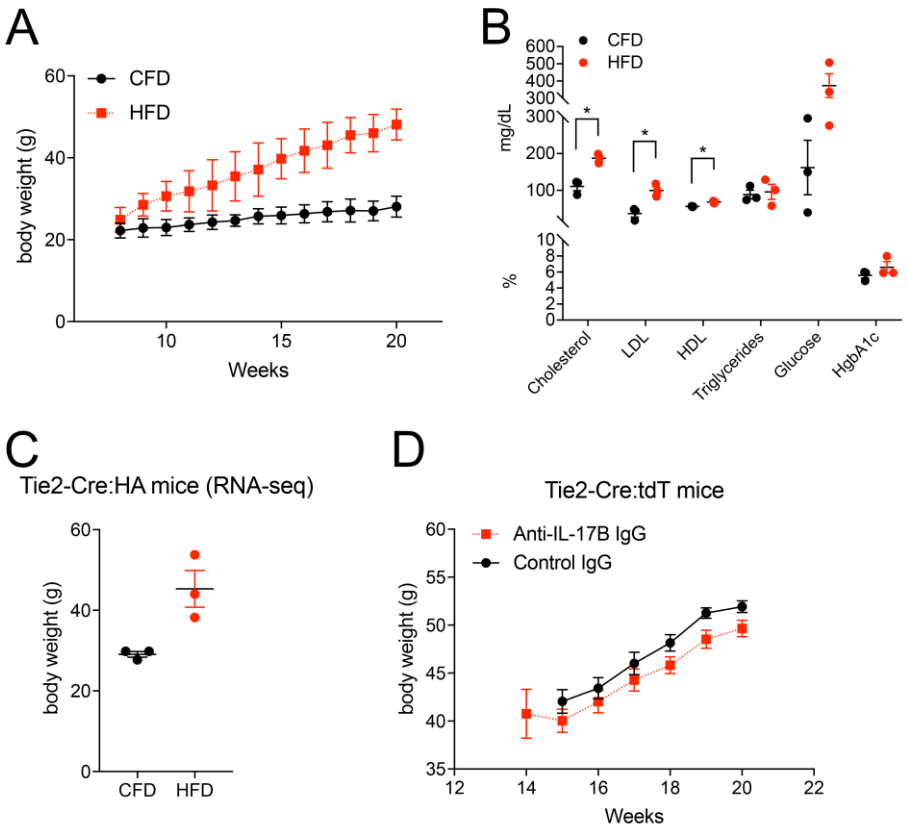

Supplemental Figure 1. High fat diet induces obesity in mice.
Week by week body weight measurements of C57BL/6J fed ad lib with CFD (black) or HFD (red) with final average 84.0% weight gain compared to 21.7% in CFD mice (***p*=0.0005; *n*=5) (A). Serologic testing of C57BL/6J mice on CFD or HFD (*n*=3) for total cholesterol (110.7±2.6 vs. 187.3±2.5; **p*=0.023), LDL (37.0 ±2.4 vs. 99.7±2.0; **p*=0.043), glucose (162.0±6.5 vs. 373.3±4.2) and HgbA1c (5.6 ±0.5vs. 6.6±0.2) (B). Final 20 week old body weights of Tie2-Cre:RiboTag HFD mice used for RNA-seq endothelial profiling (45.3±1.9 g vs. 29.1±0.6 g; *n*=3) (C). Final 20 week old body weights of Tie2-Cre;tdTomato mice fed ad lib on HFD treated with control IgG (black) and anti-IL-17B IgG (red) (51.9±0.5 g vs 49.1±0.6 g; **p*=0.029; *n*=4) (D). Data are mean ± SEM.

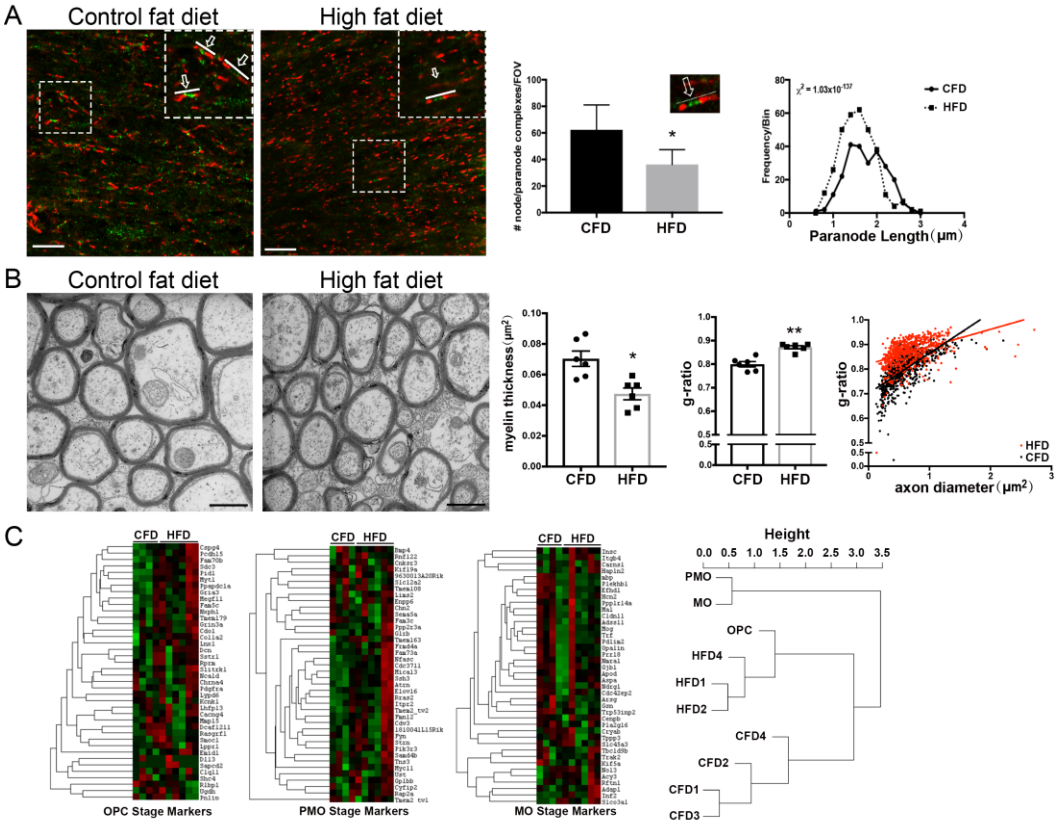

Supplemental Figure 2. Validation of white matter disruption in HFD mice.
Labeling for nodal ($Na_V1.6$, green) and paranodal (caspr, red) axonal microdomain segments within subcortical white matter in animals on CFD (left) and HFD (right). Inset boxes show examples of intact nodal and paranodal complexes (arrow with line). Average number of nodal and paranodal complexes, defined as adjacent caspr+ paranodal segments with concurrent $Na_V1.6$+ nodal segments (example in inset) (62.3±13.3 vs 36.2±7.9, ***p=1.7666 x 10^{-5}; n=2). Distribution of paranodal length (binned by 0.2 μm) in animals on HFD (dashed line) compared to CFD (solid line) demonstrating a significant left shift towards shorter paranodes in animals on HFD (1.29±0.02 μm vs 1.70±0.03 μm, Chi-square=1.7117 x 10^{-138}) (A). Callosal fibers at the midline were prepared in sagittal section for electron microscopy. Animals on CFD (n=6) demonstrated regular axonal and fiber diameter with an abundance of normally myelinated fibers (left panel, B). After 12 weeks on HFD (n=6), myelin ultrastructure in callosal fibers is compromised with reductions in myelin sheath thickness without significant changes in axonal number or fiber diameter (right panel, B). Myelin sheath thickness was significantly reduced (0.070μm vs. 0.047μm; *p=0.0087) (B). The average g-ratio was increased (0.88 vs. 0.80; **p=0.002) in animals on HFD compared to CFD (B). The distribution of axon diameter vs. g-ratio for individual axon measurements in animals on CFD (black) vs. HFD (red) showing that axon diameter was not significantly different between the groups (0.62±0.06 μm vs 0.69±0.05 μm; p=0.48) (B). Heatmap of oligodendrocyte lineage stage (OPC = oligodendrocyte progenitor cell; PMO = premyelinating oligodendrocyte; MO = myelinating oligodendrocyte) gene expression profiles (total 120 genes/40 per stage) for animals on CFD and HFD (n=4) (C), upregulated genes (red), downregulated genes (green); Hierarchical clustering of samples compared to reference marker gene expression profiles (Zhang et al. *J. Neurosci* 2014) shows that gene expression profiles of animals on HFD cluster with OPCs (C). Data are mean ± SEM. Scale bars = 10 μm (A), 1 μm (7200X magnification) (B).

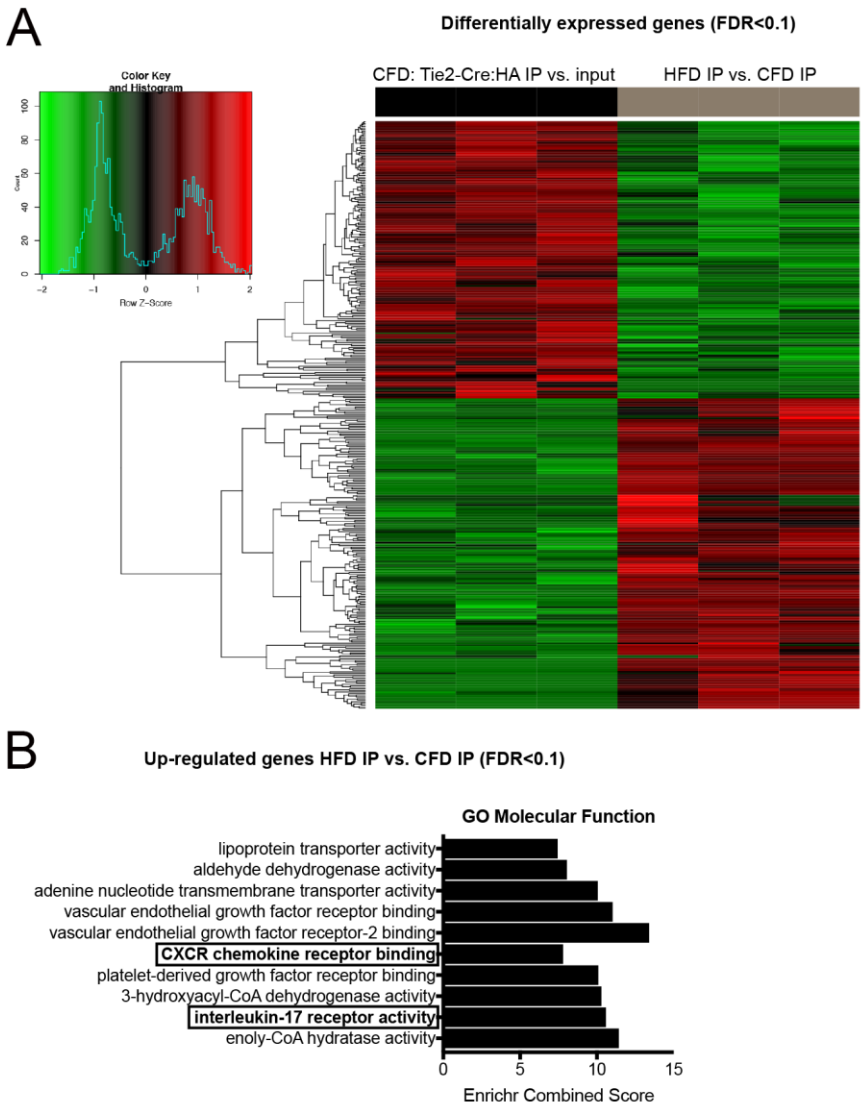

Supplemental Figure 3. DIO results in a specific white matter endothelial gene expression profile and immune signaling activation.
Heatmap representation of differentially expressed genes (FDR<0.1) between Tie2-Cre:RiboTag anti-HA immunoprecipitated ribosomes (IP) and total white matter (input) in animals on CFD (left, black) demonstrating unique transcriptional profile of white matter endothelia. Differentially expressed genes between Tie2-Cre:RiboTag anti-HA immunoprecipitated ribosomes (IP) on CFD vs. HFD (right, gray). Down-regulated genes shown in green and up-regulated genes shown in red (A). Bar plot of the Enrichr (Kuleshov et al. Nucleic Acids Res. 2016) combined score of the gene ontology (molecular function) of up-regulated genes in Tie2-Cre:RiboTag anti-HA immunoprecipitated ribosomes (IP) HFD mice indicates enrichment of immune signaling pathways including C-X-C chemokine signaling and interleukin receptor activation (B).

IL-17 family member	Log-fold change (HFD vs. CFD)	*p*-value	False discovery rate
Il17Ra	0.999	0.470	0.820
Il17Rb	**8.835**	**0.001**	**0.090**
Il17Rc	-2.695	0.303	0.695
Il17Rd	-4.038	0.043	0.397
Il17Re	2.918	0.322	0.713
Il17a	not detected	not detected	not detected
Il17b	0.000	1.000	1.000
Il17c	not detected	not detected	not detected
Il17d	-0.318	0.805	1.000
Il17f	not detected	not detected	not detected

Supplemental Table 1. Expression of IL-17 family member genes in DIO white matter endothelia from Tie2-Cre:RiboTag mice on HFD vs. CFD.

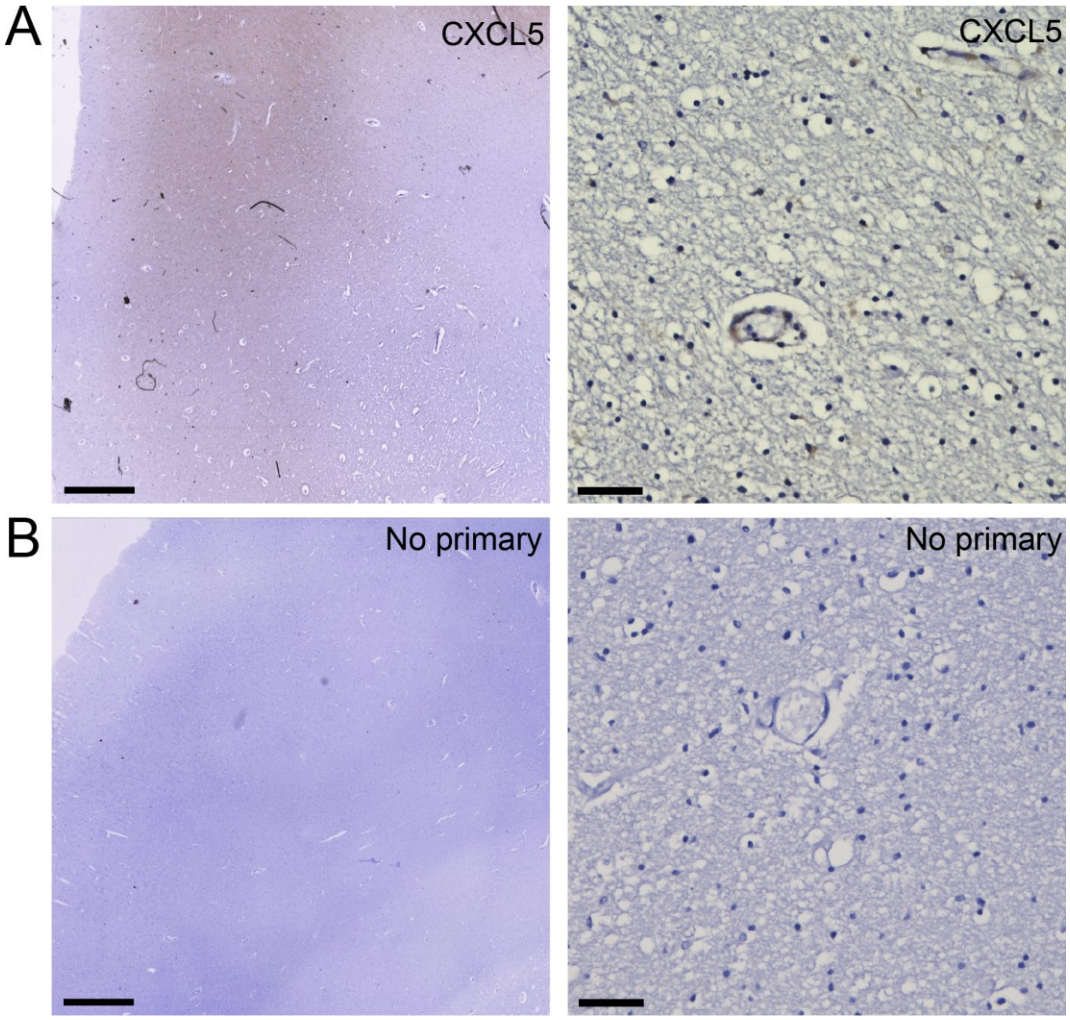

Supplemental Figure 4. Detection of CXCL5 in human peri-ventricular white matter.

Immunohistochemistry for CXCL5 in periventricular white matter reveals clear detection of CXCL5 (brown) within cortical neurons at low magnification (left panel, A)) and within endothelial cells in the white matter (right panel, A). Immunohistochemistry without anti-CXCL5 antibody demonstrates no visible staining in periventricular white matter. (B). 2X magnification (left panels, A-B) or 20X magnification (right panels, A-B). Scale bars = 200μm (left panels), 50μm (right panels).

Subject Number	Age	Sex	Ethnicity	Clinical Syndrome	Pathological Diagnosis	BRAAK	CVDSC	PMI	Any positive vessel	% positive vessel per area sampled	% positive vessel segments (number positive)
1	75	M	Hispanic	No cognitive impairment	Normal Brain	2	0	49.5	Yes	40.00%	35.3% (6)
2	83	M	White	No cognitive impairment	Possible AD (CERAD)	2	0	30	Yes	62.50%	60.0% (9)
3	96	F	White	No cognitive impairment	Normal Brain	2	0	6.9	Yes	95.00%	94.4% (17)
4	86	F	White	Questionable cognitive impairment	Vascular disease, infarcts only	1	1	-	No	0%	0% (0)
5	84	F	White	No cognitive impairment	Normal Brain	1	-	10.9	Yes	100%	100% (24)
6	72	M	White	No cognitive impairment	Vascular disease, combined lacunar and large infarctions, cerebrovascular disease	1	0	4	Yes	40.00%	50.0% (9)
7	89	M	Hispanic	Dementia	Vascular disease, multiple lacunes	2	5	69	Yes	60.00%	71.4% (15)
8	92	F	White	Dementia	Vascular disease, multiple lacunes	3	13	7	Yes	44.40%	50.0% (7)
9	90	F	Asian	Dementia	Vascular disease, Binswangers disease. Pathological findings of white matter vasculopathy	1	3	40	No	0%	0% (0)
10	92	F	Hispanic	Dementia	Limbic sclerosis, entorhinal neocortex	3	3	31	Yes	70.00%	84.6% (11)

Supplemental Table 2. Demographic and pathologic data for human post-mortem subjects.

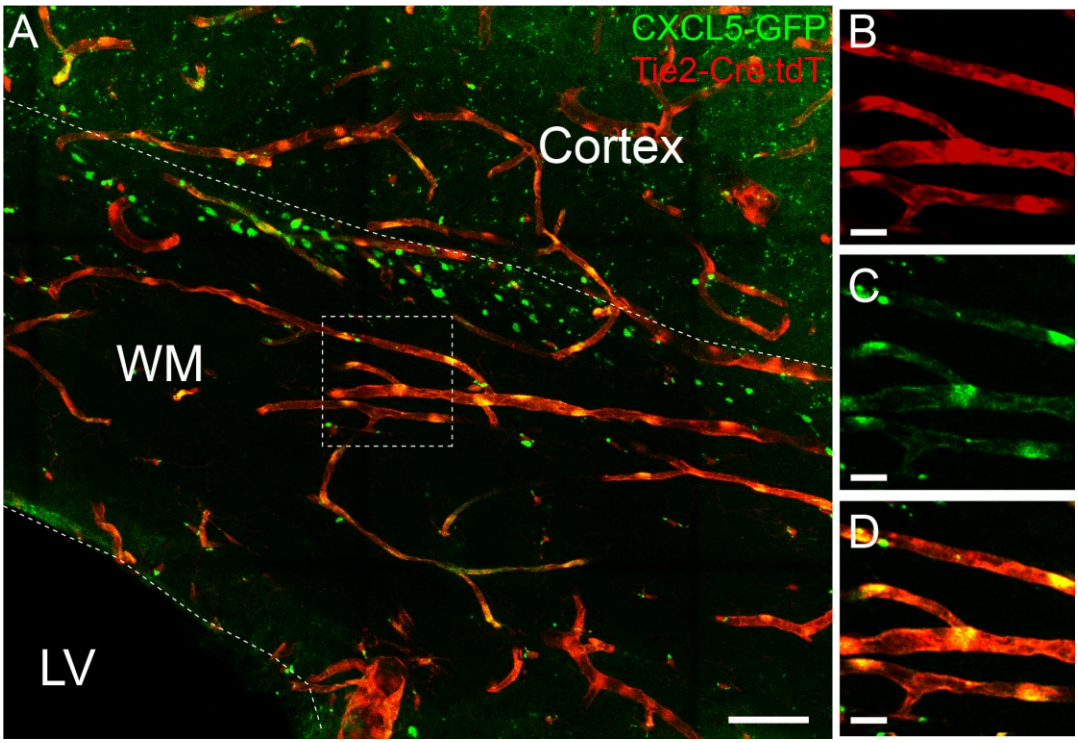

Supplemental Figure 5. Targeting of CXCL5 overexpression to white matter vasculature using combined transgenic and viral transduction.

Animals on control fat diet underwent viral transduction into the white matter with pCDH-FLEX-CXCL5-T2A-GFP (10^8 viral particles) were injected to white matter in Tie2-Cre;tdTomato mice at 14 weeks old and analyzed at 20 weeks of age (A). After 6 weeks of viral transduction, CXCL5-T2A-GFP (green) was highly colocalized with Tie2-Cre;tdTomato+ vessels (red) with the region of viral targeting in white matter (B-D). WM = white matter; LV = lateral ventricle. Scale bars = 50 μm (A), 10 μm (B-D).

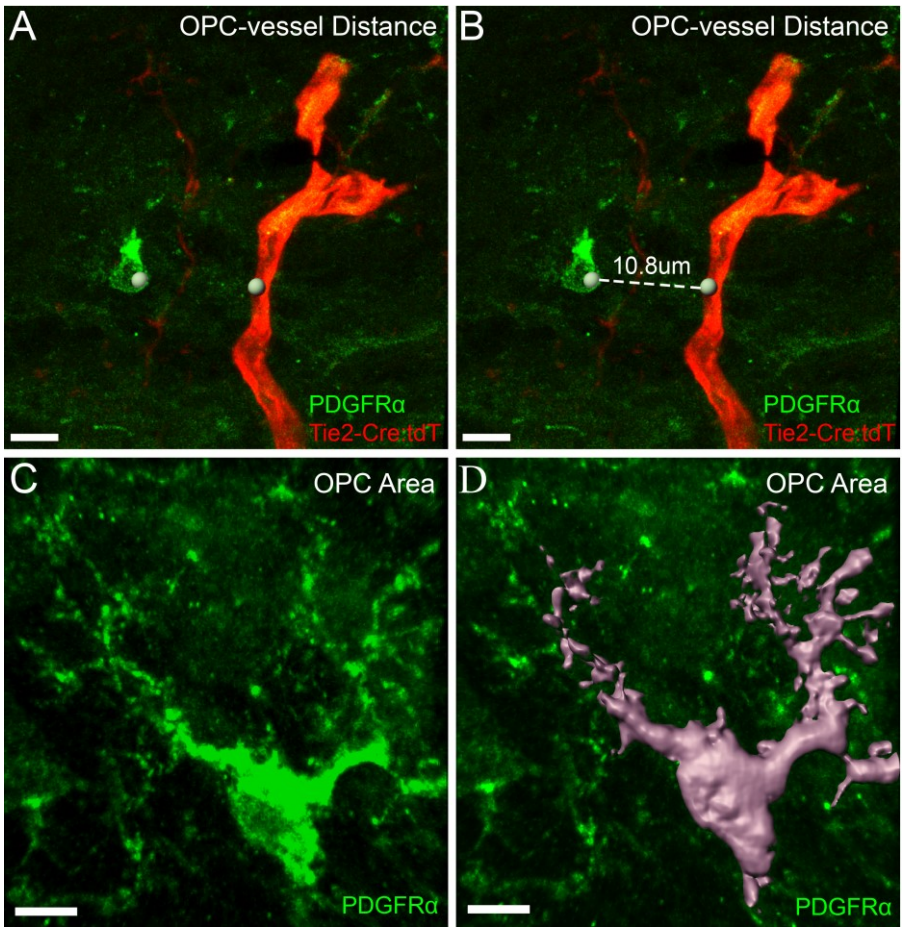

Supplemental Figure 6. Approach for measurement of OPC-vessel distance and OPC cellular area.

PDGFRα+ OPCs within 35μm range of Tie2-Cre;tdTomato+ vessel segments were identified. The linear distance between the cell body of OPC utilized as the OPC coordinate and a coordinate for the adjacent vessel was created by Imaris (A). The distance of OPC to vessel was measured (B). The cellular area of PDGFRα+ OPCs (C) were masked by Imaris with "Add surface" function to create an area measurement (μm^2) (D). Scale bar = 5 μm.

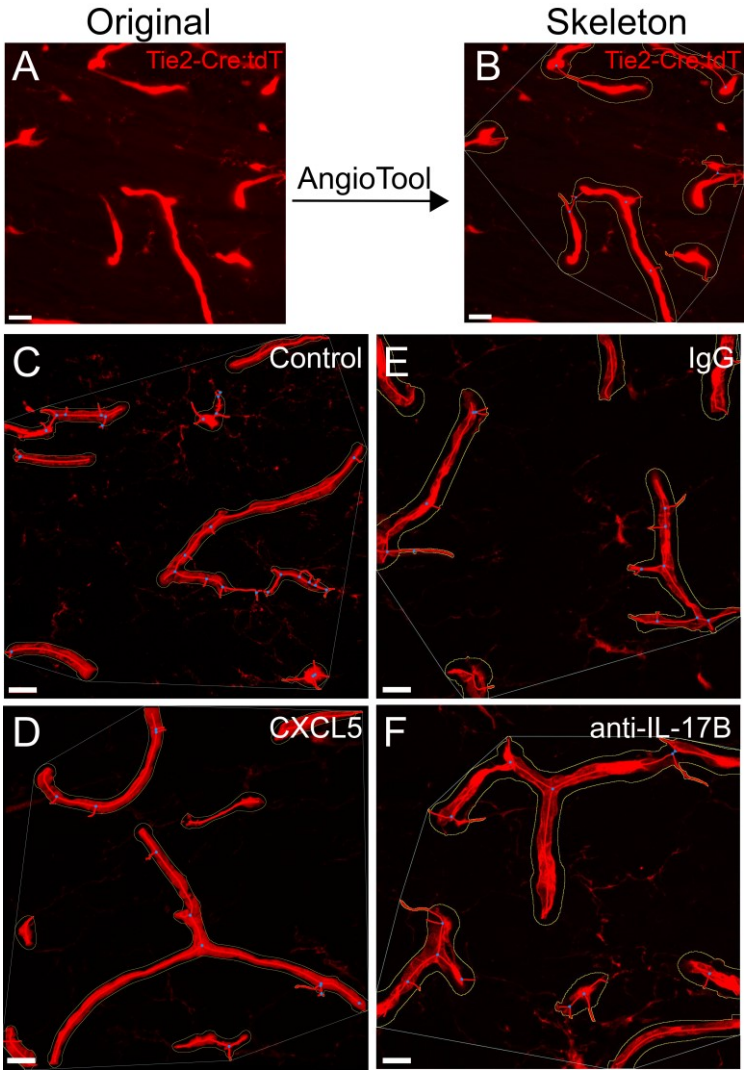

Treatment	Vessel Length (mm)	SEM	*P-value*
Control (GFP)	0.257216686	0.053521	0.891901056
CXCL5-GFP	0.253844777	0.05808	
IgG	0.218490871	0.037066	0.504302562
anti-IL-17B	0.207364	0.040578	

Supplemental Figure 7. Measurement of microvascular length using AngioTool.

The total vessel length of Tie2-Cre;tdTomato+ vessels were analyzed by AngioTool. The original high magnification tdT+ image from callosal white matter (A) was skeletonized in AngioTool which preserves contiguous vessel segments (outlines) and identifies branch points/junctions (blue dots) (B). Representative AngioTool vessel skeletons from animals on Tie2-Cre:FLEX-GFP expressing animals (C), Tie2-Cre:FLEX-CXCL5-T2A-GFP expressing animals (D), and animals on high fat diet administered either control IgG for 6 weeks (E) or anti-IL-17B IgG for 6 weeks (F). Average total vessel length of each treatment analyzed by AngioTool was shown in table. Data are mean ± SEM; Scale bar = 20 μm.

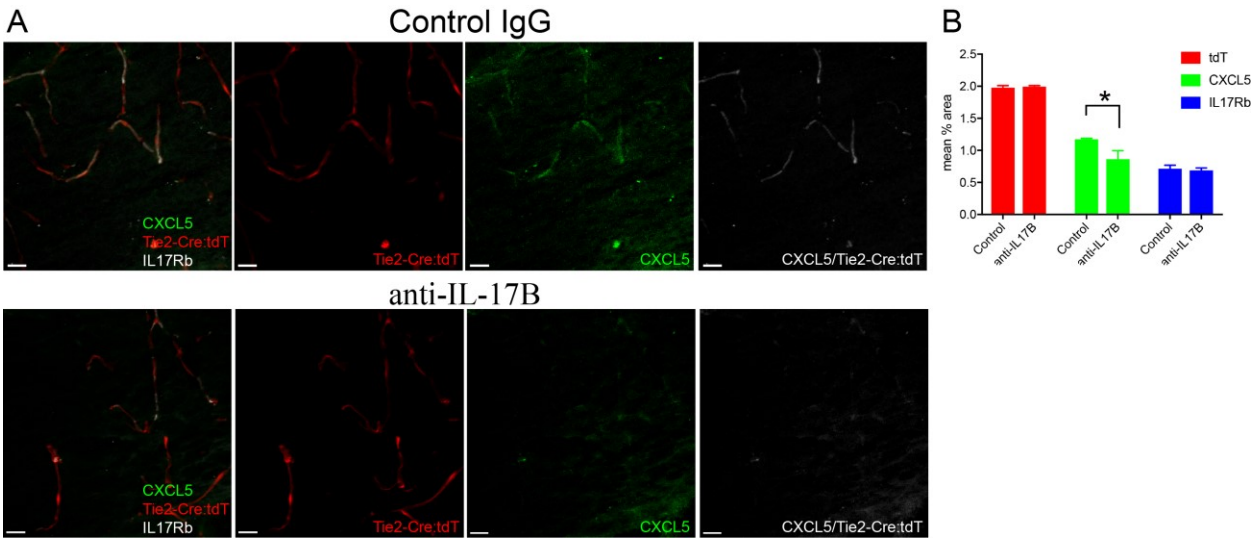

Supplemental Figure 8. Function blocking anti-IL-17B IgG reduces CXCL5 expression in Tie2-Cre;tdTomato+ white matter vasculature.

After q3d administration of function blocking anti-IL-17B IgG or control isotype-matched IgG for 6 weeks in Tie2-Cre;tdTomato animals on HFD, immunolabeling for CXCL5 (green) and IL17Rb (white) was performed. In white matter tdT+ vasculature, both CXCL5 and IL17Rb were colocalized with Tie2-Cre;tdTomato+ vessels. Using Imaris, CXCL5+ voxels that co-localized with tdT+ voxels were identified and presented in Figure 4 (A). Compared to animals administered control IgG (upper panels), mean % area occupied by immunolabeling of CXCL5 was significantly reduced in animals administered anti-IL-17B IgG (1.17 vs. 0.86; **p*=0.0067; *n*=4) (B). Endothelial expression of IL17Rb (mean % area) was not significantly different between control IgG and anti-IL-17B IgG indicating that receptor expression was not altered by anti-IL17B IgG administration. Scale bar = 20 μm, Data are mean ± SEM.

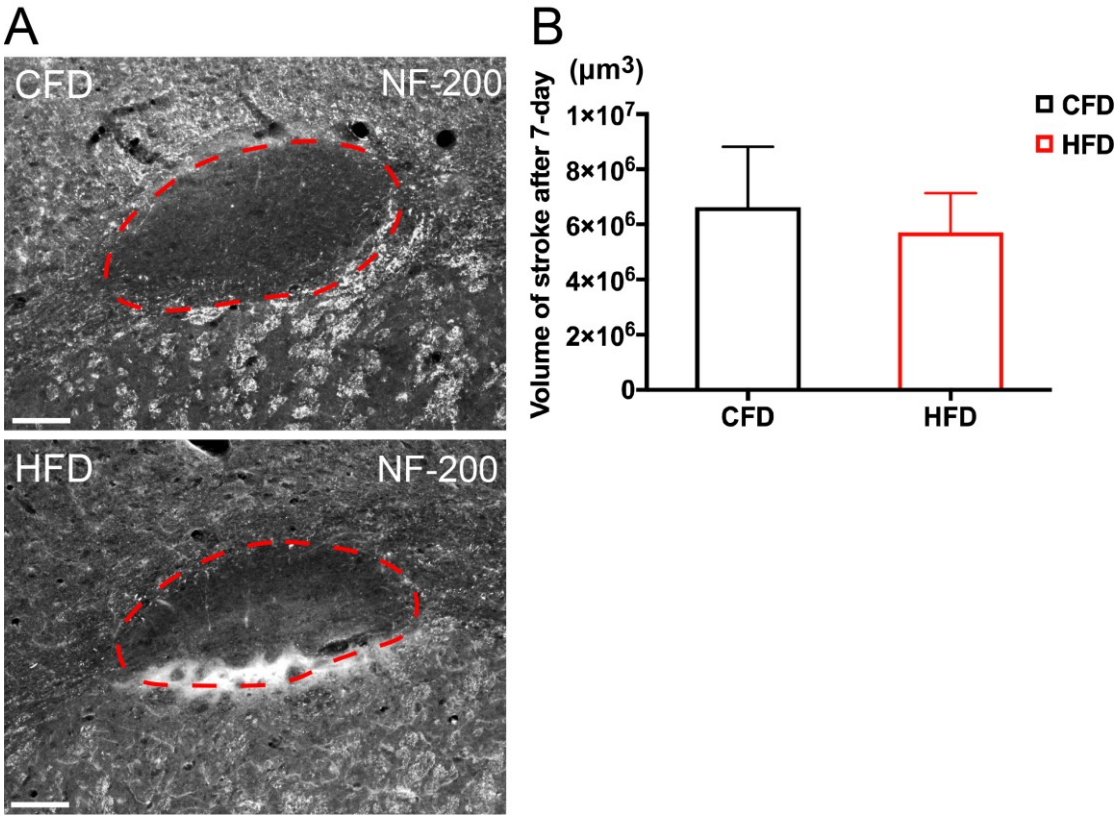

Supplemental Figure 9. Effect of diet-induced obesity on white matter stroke volume.

White matter stroke was induced as described producing a focal ischemic lesion precisely localized to subcortical white matter. The region of focal ischemia was identified by the absence of NF-200 axonal staining (A). Compared to animals on control fat diet (A), there was no significant difference between the region of axonal loss in animals on high fat diet (B). The elliptical volume of the stroke lesion was determined 7 days after stroke using formula $\pi/6 \times major\ axis \times vertical\ axis \times minor\ axis$ ($6.6 \times 10^6 \pm 604.0$ vs. $5.7 \times 10^6 \pm 485.8$ μm^3, $n=6$) (B). Scale bar = 100 μm. Data are mean ± SEM.

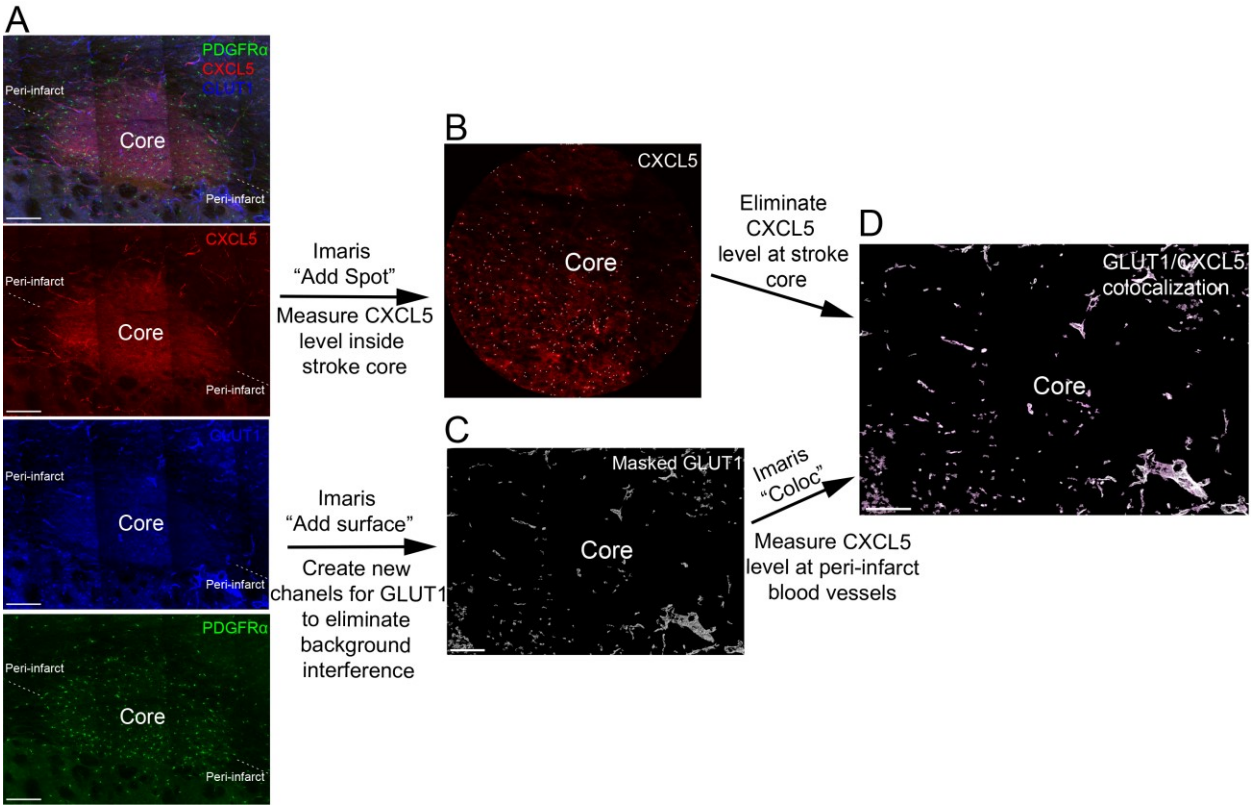

Supplemental Figure 10. Workflow to measure peri-infarct vascular CXCL5 expression.

Seven days after focal white matter ischemia, sections containing focal stroke lesions were identified and immunolabeled for PDGFRα+ (green), CXCL5 (red), and GLUT-1 (blue) to label OPCs, CXCL5, and white matter vasculature, respectively. Images containing the stroke lesion and 100 μm of surrounding peri-infarct tissue were captured using confocal microscopy (3 sections per animal*, n=2).* CXCL5 (red) was highly expressed both inside stroke core and within GLUT1+ (blue) blood vessels in the surrounding peri-infarct regions (A). The stroke core was identified by a marked increase in stroke-responsive PDGFRα+ OPCs (green) and a paucity of GLUT-1 staining. The levels of CXCL5 inside the segmented stroke core were measured by Imaris "Add spot" function and removed from analysis because it represented CXCL5 expression by infiltrating inflammatory cells (B). To measure the expression level of CXCL5 by endothelial cells within peri-infarct vasculature, GLUT1+ vessels were masked by Imaris "Add surface" function (C). Using Imaris software, a new channel of CXCL5 expression co-localized with the masked GLUT1+ surface was created. The expression levels of CXCL5 within GLUT1+ vessels, largely restricted to the peri-infarct regions, were analyzed by Imaris "Coloc" function (D) and quantified between animals on CFD vs. HFD (Fig. 5B). Scale bar = 100 μm.

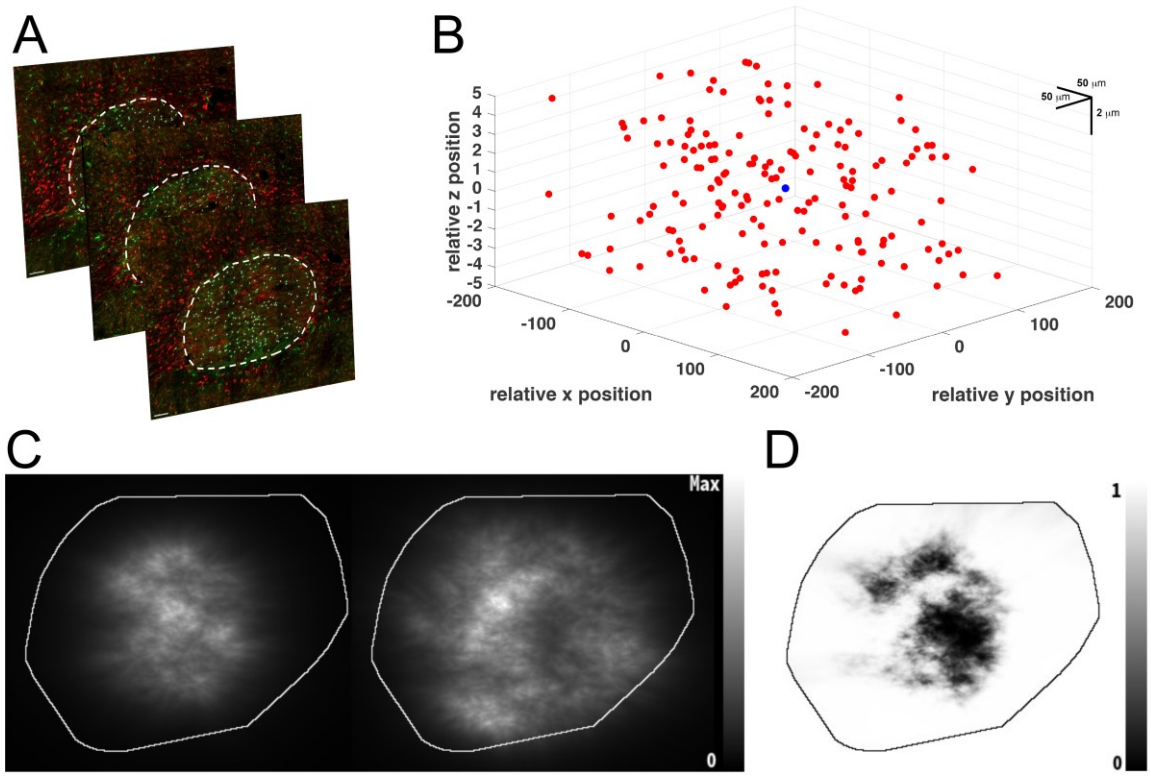

Supplemental Figure 11. Spatial mapping of stroke-responsive OPCs.
Confocal z-stacks through the white matter stroke lesion were used to identify stroke-responsive PDGFRα+ OPCs (green) within the lesion core where GST-π+ mature oligodendrocytes (red) were lost due to focal ischemia (11 steps of Z-stacks per image) (A). Spatial coordinates of each cell (*x,y,z* in µm) relative to the center point of the stroke lesion (blue dot) were used to generate spatial maps of stroke-responsive OPCs (red) within each lesion section (insert number of sections per group; total cells measured). Representative coordinate map of stroke-responsive OPC localization from one section (B). Average OPC spatial density maps were generated in 2D for animals on CFD (left, *n*=3) and those on HFD (right, *n*=3) as described (J. Burguet et al Pattern Recogn Lett, 2011). Vertical gray bar represents cellular density with max density value = 3.97×10^{-3} cells/µm^2. Curve in white: ROI contour (C). Map of *p*-values for differences in stroke-responsive OPC densities between animals on CFD and HFD. Vertical gray bar represents *p*-value. Low *p*-values (<0.05; black) correspond to regions with significantly more cells in the control group, and high *p*-values (>0.95; white) to regions with significantly more cells in the HFD group. Stroke-responsive cellular density per lesion was significant higher within the peripheral aspects of the lesion in animals on HFD compared to CFD (D). Scale bar in A = 50 µm.

References

[1] J. D. Hinman, M. N. Rasband, and S. T. Carmichael, "Remodeling of the axon initial segment after focal cortical and white matter stroke," *Stroke*, 2013.

[2] E. Zudaire, L. Gambardella, C. Kurcz, and S. Vermeren, "A computational tool for quantitative analysis of vascular networks," *PLoS One*, vol. 6, no. 11, Nov. 2011.

[3] J. Schindelin *et al.*, "Fiji: an open-source platform for biological-image analysis.," *Nat. Methods*, 2012.

[4] E. G. Sozmen *et al.*, "Nogo receptor blockade overcomes remyelination failure after white matter stroke and stimulates functional recovery in aged mice," *Proc. Natl. Acad. Sci.*, vol. 113, no. 52, pp. E8453–E8462, Dec. 2016.

[5] E. Sanz, L. Yang, T. Su, D. R. Morris, G. S. McKnight, and P. S. Amieux, "Cell-type-specific isolation of ribosome-associated mRNA from complex tissues," *Proc. Natl. Acad. Sci.*, 2009.

[6] G. W. Gundersen *et al.*, "GEO2Enrichr: Browser extension and server app to extract gene sets from GEO and analyze them for biological functions," *Bioinformatics*, 2015.

[7] Y. Zhang *et al.*, "An RNA-Sequencing Transcriptome and Splicing Database of Glia, Neurons, and Vascular Cells of the Cerebral Cortex," *J. Neurosci.*, 2014.

[8] J. Burguet, Y. Maurin, and P. Andrey, "A method for modeling and visualizing the three-dimensional organization of neuron populations from replicated data: Properties, implementation and illustration," *Pattern Recognit. Lett.*, 2011.

[9] J. Burguet and P. Andrey, "Statistical comparison of spatial point patterns in biological imaging," *PLoS One*, 2014.